





RESEARCH ARTICLE | OCTOBER 07 2024

Posterior comparison of model dynamics in several hybrid turbulence model forms

Colin A. Z. Towery  ; Juan A. Sáenz  ; Daniel Livescu  



Physics of Fluids 36, 105148 (2024)

<https://doi.org/10.1063/5.0228561>



Articles You May Be Interested In

KoopmanLab: Machine learning for solving complex physics equations

APL Mach. Learn. (September 2023)

Experimental realization of a quantum classification: Bell state measurement via machine learning

APL Mach. Learn. (September 2023)



APL Quantum
Latest Articles Now Online
Read Now



Posterior comparison of model dynamics in several hybrid turbulence model forms

Cite as: Phys. Fluids **36**, 105148 (2024); doi: [10.1063/5.0228561](https://doi.org/10.1063/5.0228561)

Submitted: 13 July 2024 · Accepted: 13 September 2024 ·

Published Online: 7 October 2024



View Online



Export Citation



CrossMark

Colin A. Z. Towery,^{a)} Juan A. Sáenz,^{b)} and Daniel Livescu^{c)}

AFFILIATIONS

Los Alamos National Laboratory, Los Alamos, New Mexico 87545, USA

^{a)}Electronic mail: colin.towery@gmail.com

^{b)}Electronic mail: juan.saenz@lanl.gov

^{c)}Author to whom correspondence should be addressed: livescu@lanl.gov

ABSTRACT

Hybrid turbulence models that can accurately reproduce unsteady three-dimensional flow physics across the entire range of grid scales and turbulence dynamics from Reynolds-averaged Navier–Stokes (RANS), through large-eddy simulation (LES), down to direct numerical simulations (DNS) are of increasing interest to the turbulence modeling community. However, despite decades of research and development, the basic tasks of eliminating poor-performing hybrid RANS-LES models and accelerating adoption of superior models through well-designed validation and verification have yet to occur. As a step in this direction, in this work we evaluate thirteen different hybrid RANS-LES models via systematic grid refinement of decaying homogeneous isotropic turbulence. We further derive a novel mathematical framework for assessing the energy partitioning dynamics of each Hybrid RANS-LES model, wherein model-to-model variations in energy partitioning can be interpreted as different feedback mechanisms operating on a low-dimensional nonlinear dynamical system. We found that model forms similar to the flow simulation methodology—also often termed very-large eddy simulation—are dynamically inconsistent with DNS at all resolutions. Additionally, we found a strong dynamical similarity in the feedback mechanisms of all models related to detached eddy simulation and partially averaged Navier–Stokes that is inherent to their general model forms.

© 2024 Author(s). All article content, except where otherwise noted, is licensed under a Creative Commons Attribution-NonCommercial 4.0 International (CC BY-NC) license (<https://creativecommons.org/licenses/by-nc/4.0/>). <https://doi.org/10.1063/5.0228561>

I. INTRODUCTION

Modeling turbulent flow phenomena is a critical aspect of understanding and predicting a myriad of important engineering and scientific problems (e.g., aerodynamics,¹ wind energy,² nuclear fusion experiments,^{3–5} earth system,⁶ and astrophysics⁷). In most applications, turbulent flows are challenging to model computationally due to non-equilibrium dynamics, significant three-dimensional (3D) inhomogeneous features, and very large ranges in characteristic dimensional scales. Reynolds-averaged Navier–Stokes (RANS) models of turbulence, which are the state-of-the-practice for engineering design, are capable of capturing flows with very large ranges in characteristic dimensional scales (e.g., very high Reynolds numbers, Re). However, unsteady RANS simulations (URANS) perform poorly for simultaneously non-stationary and inhomogeneous flows, where there is a lack of conceptual clarity regarding what properly constitutes an ensemble-average solution to the Navier–Stokes equations.⁸ In contrast, well-resolved large-eddy simulations (LES), which seek a spatially filtered solution to the Navier–Stokes equations and are the

state-of-the-art in 3D inhomogeneous turbulence modeling, are computationally inaccessible for flows with very large Re .

For these reasons, a great number of *hybrid RANS-LES* (HRL) modeling concepts have appeared in academic and commercial use over the last few decades. These wide-ranging efforts are united by the shared objective to combine the best aspects of both RANS and LES in order to accurately reproduce unsteady 3D flow physics at an affordable computational cost. However, there is significant diversity in the mathematical methods and theoretical or practical justifications underpinning these various hybrid models, and much work has been done simply to catalog and group together similar concepts. (We recommend Fröhlich and Von Terzi,⁹ Sagaut *et al.*,¹⁰ Chaouat,¹¹ and Heinz¹² for a comprehensive survey of HRL concepts and their categorizations.) For instance, HRL concepts are generally categorized by general traits such as “zonal” methods, which switch between distinct URANS and LES models based on a user-prescribed location within the domain (e.g., distance from a wall), “blended” methods, which combine separate RANS and LES model stresses at all grid points, or

“unified” models, which output a single turbulence stress at all points from a single set of model equations that exhibit aspects of both the RANS and LES modeling paradigms. We take care to distinguish between our use of the very similar terms URANS and RANS. Within this paper, RANS refers to the general mathematical model form, which may be potentially utilized in an HRL concept to directly compute LES-like solutions that resolve turbulence fluctuations. In contrast, URANS will always refer specifically to computations seeking a statistical-average solution.

The most widely utilized HRL methods are all unified models that could be applied to any turbulence flow regime, wall-bounded or free, and including flows that lack a definable statistical average flow field. These models are also able to span the entire range of turbulence scales between URANS and direct numerical simulation (DNS)—where the full 3D and time-resolved variability of the turbulent fluctuations is computed. Such HRL models are often referred to collectively as scale-resolving simulations (SRS)^{13,14} and include the various detached eddy simulation (DES) models,^{1,15} the functionally equivalent partially averaged Navier–Stokes (PANS)^{16,17} and partially integrated transport (PITM)^{18,19} models, and the loose family of flow simulation methodology (FSM)^{20,21} and very large eddy simulation (VLES) models. These unified SRS models are the main modeling subject of this work.

A strong motivation for most, if not all, HRL concepts is that URANS near-wall modeling significantly outperforms resolved LES in both accuracy and cost for attached boundary layers. Much time and attention has been paid to the algorithmic and computational-grid interfaces between URANS-based near-wall approximations and “free-stream” turbulence closures of all kinds—whether another RANS model,²² HRL model,¹⁵ or LES model.²³ However, wall models are generally interchangeable and can be added as an algorithmic extension to any underlying turbulence model. Therefore, it would be more apt to describe practical HRL models as a triple combination of near-wall, RANS, and LES capabilities. Unfortunately, the potential deficiencies of HRL model performance in unbounded flow regimes are routinely under-emphasized due to a persistent and widespread focus on testing model performance in wall-bounded industrial and aerospace flows. This has caused a tendency to conflate the separable aspects of model performance in near-wall flow regions—where the specific wall model treatments and variations in grid structure determine overall accuracy—and model performance far from walls or in boundary-free flows (e.g., Rayleigh–Taylor or shear driven mixing, jets, wakes)—where grid resolutions tend to be much coarser, Re much higher, and grid structures more uniform and isotropic.

Such a strong focus on boundary-layer-driven, complex flow cases have limited the development of formal verification and validation (V&V) procedures for HRL models.^{13,14} Errors in computations of these flows are usually dominated by the choice of specific wall function and near-wall grid structure, with overlapping model-form and numerical errors propagating from boundary layers into the free-stream regions of the flow. In these cases, it is impossible to unambiguously evaluate the performance of the underlying HRL model, and the objective comparison of several models head-to-head within a single computational code is rarely presented. A systematic comparison of several HRL models within a single numerical code based on canonical flow cases free from these near-wall modeling influences can focus on assessing model-form error while explicitly controlling for errors and

uncertainties due to numerical discretization and the experimental initial and boundary conditions. Therefore, we address two objectives in this study: to develop a formal validation methodology for assessing SRS model-form errors in unbounded flow conditions and to uniformly apply this methodology to a wide range of models using a single computational code with minimal numerical error.

Perhaps the most basic approach to assessing model error is to determine if an HRL solution is consistent with the true Navier–Stokes dynamics coarse-grained by a spatiotemporal filter operation. Friess *et al.*²⁴ refer to this expectation as an HRL model’s *self-consistency* with the resolved turbulence it captures as the notional filter width is systematically varied between URANS and DNS as part of the V&V procedure. Furthermore, an HRL model should satisfy this expectation even if the model is not *explicitly* based on the filtered Navier–Stokes equations, as in traditional LES, by enforcing the partitioning of turbulence kinetic energy between resolved and modeled components that is dynamically consistent with the *implied* filtering operation arising from each unique combination of computational grid widths, time step sizes, initial and boundary conditions, and scale-determining model coefficient values.¹⁴ Both Chaouat¹¹ and Heinz¹² similarly emphasize the correct partitioning of kinetic energy as both the primary *a priori* modeling objective and a *posteriori* diagnostic criterion for assessing model dynamics.

In the present study, we choose to evaluate HRL model energy partitioning dynamics via systematic grid refinement of decaying homogeneous isotropic turbulence (HIT). Decaying HIT is an excellent minimum working example as all two-equation, linear eddy viscosity RANS models reduce to an equivalent system of ordinary differential equations. In fact, $k-\omega$, $k-\tau$, $k-L$, etc., can all be derived algebraically from the $k-\epsilon$ model for homogeneous turbulence cases, and the URANS $k-\epsilon$ equations can very well model a power-law decay process in isotropic turbulence. More complicated flow cases should be considered in a comprehensive V & V plan; however, our choice to use decaying HIT as the test case allows for a consistent assessment of modeling error using a single minimal-error numerical implementation. Additionally, demonstrating self-consistency for HIT improves overall confidence in SRS-type HRL models.

We evaluate the posterior performance of thirteen distinct SRS-type HRL models that can be derived from the $k-\epsilon$ RANS model. We classify these as either DES-like, PANS-like, or FSM-like models. The energy-partitioning dynamics of these HRL models are evaluated against both the filtered DNS truth as well as the dynamics of two control models: the standard $k-\epsilon$ (SKE) RANS model and a one-equation subgrid-scale (SGS) LES model, i.e., a constant-coefficient k -SGS model. The SKE model, tested as an HRL model and not as a URANS, is the *mathematical baseline* that each true HRL model directly modifies in some way. The k -SGS LES model, which is essentially the k -equation of SKE with a simplified algebraic model for ϵ , acts as a *performance baseline* for assessing the relative accuracy of each HRL model in comparison with a traditional LES model. We have not chosen to use as a control any of the more common algebraic LES models,²⁵ such as Dynamic Smagorinsky, since these models do not provide a solution for the subgrid-scale kinetic energy and are, therefore, unsuitable for evaluations of energy partitioning dynamics.

In Sec. II, we first introduce the concept of power-law decay in HIT and how it can be modeled by $k-\epsilon$ URANS. Second, we present a single set of generalized $k-\epsilon$ governing equations that can be used to

classify HRL models as DES-like, PANS-like, or FSM-like according to the coefficients they modify. We then introduce each of the thirteen HRL models to be tested in this study and classify them in the aforementioned three major classes. Finally, we derive a set of non-dimensional differential equations for the evolution of the power-law exponents of the resolved and modeled kinetic energies that can be used to sensibly compare model dynamics of decaying HIT across all times, filter scales, and energy partitioning levels. In section III, we describe the minimal-error pseudospectral solution method employed for every simulation—whether DNS, LES, RANS, or HRL. Following that, we present detailed results of the energy partitioning dynamics for each model, and we compare and contrast the differing nonlinear feedback mechanisms that each major HRL class (i.e., DES, PANS, and FSM) induces to modify the baseline SKE dynamics. Finally, we summarize and conclude our important findings.

II. THEORY AND GOVERNING EQUATIONS

In the present simulations, incompressible and isotropic turbulence (HIT) is represented by the Navier–Stokes equations subject to specific initial and boundary conditions, as given by

$$\frac{\partial u_i}{\partial t} + u_j \frac{\partial u_i}{\partial x_j} = \frac{\partial}{\partial x_j} (-p\delta_{ij} + 2\nu S_{ij}), \quad (1)$$

where u_i is the velocity vector, p is the dynamic pressure divided by the constant fluid density, ν is the kinematic viscosity, and $S_{ij} = \frac{1}{2}(\partial u_i/\partial x_j + \partial u_j/\partial x_i)$ is the strain tensor. Decaying HIT has zero mean velocity, $\langle u_i \rangle = 0$ as well as zero mean spatial gradients, $\partial \langle \cdot \rangle / \partial x_j = 0$, including $\langle S_{ij} \rangle$, where $\langle \cdot \rangle$ denotes the spatial (Reynolds) average of a quantity, and thus, the mean turbulence quantities depend only on time. In particular, the mean turbulent kinetic energy (TKE), $\mathcal{K}_t = \frac{1}{2} \langle u_i u_i \rangle$, and mean viscous dissipation, $\mathcal{E}_t = 2\nu \langle S_{ij} S_{ij} \rangle$, are theorized to conform to a power law solution,²⁶

$$\mathcal{K}_t = \mathcal{K}_{t,0} \left(1 + \frac{t}{n\tau_0} \right)^{-n}, \quad (2a)$$

$$\mathcal{E}_t = \mathcal{E}_{t,0} \left(1 + \frac{t}{n\tau_0} \right)^{-(n+1)}, \quad (2b)$$

where $\tau_0 = \mathcal{K}_{t,0}/\mathcal{E}_{t,0}$ is the integral timescale at the start of decay ($t = 0$) and n is the exponential decay rate. Dividing Eq. (2a) by (2b) gives $\mathcal{K}_t/\mathcal{E}_t = \tau_0 + t/n$, and so, n can be determined from DNS data by a simple linear least squares fit.

The power-law decay process can also be described by simple linear ordinary differential equations (ODEs), which are derived by substituting the non-dimensional decay time, $t' = 1 + t/n\tau_0$, into Eq. (2), taking the logarithm of both sides, and then differentiating with respect to $\ln t'$,

$$\frac{d \ln \mathcal{K}_t}{d \ln t'} = -n, \quad \frac{d \ln \mathcal{E}_t}{d \ln t'} = -(n+1). \quad (3)$$

The standard k - ε URANS model of HIT is a coupled system of nonlinear ODEs,

$$\frac{d\mathcal{K}_t}{dt} = -\mathcal{E}_t, \quad (4a)$$

$$\frac{d\mathcal{E}_t}{dt} = -C_{\varepsilon 2} \frac{\mathcal{E}_t^2}{\mathcal{K}_t}, \quad (4b)$$

where $C_{\varepsilon 2}$ is a free model constant. $C_{\varepsilon 2}$ can be related to n by applying the chain rule for differentiation,

$$\frac{d \ln y}{d \ln t'} = \left(\frac{1}{t'} \frac{dt'}{dt} \right)^{-1} \frac{1}{y} \frac{dy}{dt} = \frac{t + n\tau_0}{y} \frac{dy}{dt},$$

to Eq. (4)

$$\frac{d \ln \mathcal{K}_t}{d \ln t'} = -(t + n\tau_0) \frac{\mathcal{E}_t}{\mathcal{K}_t} = -n, \quad (5a)$$

$$\frac{d \ln \mathcal{E}_t}{d \ln t'} = -C_{\varepsilon 2} (t + n\tau_0) \frac{\mathcal{E}_t}{\mathcal{K}_t} = -C_{\varepsilon 2} n. \quad (5b)$$

and comparing the result to Eq. (3). Equations (5a) and (5b) are clearly equivalent ODEs, differing only by the constant multiplier $C_{\varepsilon 2} = (n+1)/n$. The various steps required to relate $C_{\varepsilon 2}$ to n , when taken in a different order, can actually be used *a priori* as a partial derivation of the standard k - ε RANS model.

Though mean turbulence quantities in decaying HIT are dependent only on time, the local and instantaneous turbulence fluctuations remain three-dimensional quantities in space that can be filtered, resulting in the partition of TKE into resolved and modeled (subgrid-scale) energies. When a convolutional spatial filter, denoted by $\bar{\cdot}$, is applied to Eq. (1), the filtered Navier–Stokes equation is given as

$$\frac{\partial \bar{u}_i}{\partial t} + \bar{u}_j \frac{\partial \bar{u}_i}{\partial x_j} = \frac{\partial}{\partial x_j} (-\bar{p}\delta_{ij} + 2\nu \bar{S}_{ij} - \tau_{ij}), \quad (6)$$

where $\tau_{ij} = \overline{u_i u_j} - \bar{u}_i \bar{u}_j$ is the turbulence stress, and half its trace is the modeled kinetic energy $k_m = \frac{1}{2} \tau_{ii}$. The resolved kinetic energy is $k_r = \frac{1}{2} \bar{u}_i \bar{u}_i$, and the average of their sum is total TKE, $\mathcal{K}_t = \mathcal{K}_m + \mathcal{K}_r = \langle k_m \rangle + \langle k_r \rangle$. The mean dissipation can be similarly partitioned as $\mathcal{E}_t = \mathcal{E}_m + \mathcal{E}_r = \langle \varepsilon_m \rangle + \langle \varepsilon_r \rangle$, where $\varepsilon_r = \nu |\bar{S}|^2$, $\varepsilon_m = \nu (|\bar{S}|^2 - |\bar{S}|^2)$, and $|\bar{S}| = (2S_{ij} S_{ij})^{1/2}$. The partition of mean TKE between resolved and modeled components in decaying HIT is governed solely by viscous dissipation and the cross-scale energy transfer term $\Pi = -\tau_{ij} \bar{S}_{ij}$,

$$\frac{d\mathcal{K}_r}{dt} = -\langle \Pi \rangle - \mathcal{E}_r, \quad (7a)$$

$$\frac{d\mathcal{K}_m}{dt} = \langle \Pi \rangle - \mathcal{E}_m, \quad (7b)$$

where the sum of Eqs. (7a) and (7b) reduces to Eq. (4a).

The notion that a single turbulence model can be general enough to be valid for any physical fidelity between URANS and DNS is supported by several studies. Germano²⁷ introduced the concept of generalized central moments, demonstrating that the filtered Navier–Stokes equations have the same mathematical form as their Reynolds-averaged counterparts. Saenz *et al.*²⁸ further extended Germano's formalism to two-point, positive-definite filter kernels applied to variable-density turbulence and demonstrated that various central moments for the filtered variable-density NS equations and their realizability conditions converge to the corresponding URANS equations and realizability conditions, in the limit of large filter widths along directions of homogeneity. Therefore, the spatial filter operator, $\bar{\cdot}$, could be interchanged with the Reynolds average operator, $\langle \cdot \rangle$, without altering the form of Eq. (6). The principal differences between LES and

RANS models lie in the physical interpretation and modeling constraints placed on the turbulence stress, τ_{ij} . In practice, LES models are functionally distinct from RANS models only in that the former are dependent on a user-defined spatial filter scale (e.g., the local computational grid width).

LES models of turbulence are largely concerned with finding model forms that give the correct average cross-scale energy transfer, $\langle \Pi_m \rangle = -\langle \tau_{ij}^m \bar{S}_{ij} \rangle \approx \langle \Pi \rangle$, where Π_m and τ_{ij}^m denote the modeled values while the true Π value can be determined from DNS data. Most typical LES models, like their RANS counterparts, are linear eddy viscosity models that prescribe the form $\tau_{ij}^m = -2\nu_m \bar{S}_{ij} + \frac{2}{3}k_m \delta_{ij}$, where ν_m is the model's eddy viscosity. For example, the one-equation k -SGS model—a very useful baseline LES model to compare against DES modeling—sets $\nu_m = C_m \Delta \sqrt{k_m}$ and solves a transport equation for k_m ,

$$\frac{\partial k_m}{\partial t} + \bar{u}_j \frac{\partial k_m}{\partial x_j} = \Pi_m - \varepsilon_m + \frac{\partial}{\partial x_j} \left[\left(\nu + \frac{\nu_m}{\sigma_k} \right) \frac{\partial k_m}{\partial x_j} \right], \quad (8)$$

which is closed by $\Pi_m = \nu_m \bar{S}^2$ and $\varepsilon_m = C_\varepsilon k_m^{3/2} / \Delta$, where Δ is the uniform grid scale. The model coefficients C_m , C_ε , and σ_k are constants that can be determined empirically from a reference DNS simulation or using a dynamic procedure. A complete accounting of the historical development, theoretical justification, and possible alternative dynamic coefficients for the k -SGS model can be found in Sagaut.²⁵

In contrast, the two-equation SKE RANS model removes any dependence on Δ (or any other resolution-like parameter) from the one-equation LES model by setting $\nu_m = C_\mu k_m^2 / \varepsilon_m$ and prescribing a full differential transport equation for ε_m ,

$$\frac{\partial \varepsilon_m}{\partial t} + \bar{u}_j \frac{\partial \varepsilon_m}{\partial x_j} = \frac{\varepsilon_m}{k_m} (C_{\varepsilon 1} \Pi_m - C_{\varepsilon 2} \varepsilon_m) + \frac{\partial}{\partial x_j} \left[\left(\nu + \frac{\nu_m}{\sigma_\varepsilon} \right) \frac{\partial \varepsilon_m}{\partial x_j} \right]. \quad (9)$$

The complete SKE model consists of both Eqs. (8) and (9), together with the constant coefficients C_μ , σ_k , σ_ε , $C_{\varepsilon 1}$, and $C_{\varepsilon 2}$. The values of these constants can be set either by theoretical considerations (e.g., requiring that $C_{\varepsilon 2}$ give a specific power-law decay rate of TKE, as above) or by empirical calibration to a reference experiment. The particular values of the SKE and k -SGS constants used here are shown in Table I. The inclusion of a C_Δ constant as a part of the definition for the k -SGS model constants is explained in Subsection II B, while the nonstandard value for $C_{\varepsilon 2}$ is explained in the methods section, Subsection III A.

To perform a URANS simulation with the SKE model, Eq. (6) would need to be solved in addition to Eqs. (8) and (9), but with all filtered quantities (e.g., \bar{u}_i , k_m , ε_m) conceptually re-interpreted as mean quantities for consistency (e.g., $\langle u_i \rangle$, \mathcal{K}_t , \mathcal{E}_t). However, no change in the mathematical form is required for the SKE model to be employed directly as a crude SRS-type HRL model. This is why, in practice, simulations intended to be URANS can easily produce local and

instantaneous turbulence fluctuations,⁸ and why we present the model using the same coarse-graining notation as for LES.

As a basis for comparison, all of the HRL models tested in this study will be presented using a single set of *generalized* k - ε transport equations,

$$\frac{\partial k_m}{\partial t} + \bar{u}_j \frac{\partial k_m}{\partial x_j} = \Pi_m - C_{k2}^* \varepsilon_m + \frac{\partial}{\partial x_j} \left[\left(\nu + \frac{\nu_m}{\sigma_k} \right) \frac{\partial k_m}{\partial x_j} \right], \quad (10a)$$

$$\frac{\partial \varepsilon_m}{\partial t} + \bar{u}_j \frac{\partial \varepsilon_m}{\partial x_j} = \frac{\varepsilon_m}{k_m} (C_{\varepsilon 1}^* \Pi_m - C_{\varepsilon 2}^* \varepsilon_m) + \frac{\partial}{\partial x_j} \left[\left(\nu + \frac{\nu_m}{\sigma_\varepsilon} \right) \frac{\partial \varepsilon_m}{\partial x_j} \right], \quad (10b)$$

where in $\nu_m = C_\mu^* k_m^2 / \varepsilon_m$, and one or more of the SKE model constant coefficients is replaced with a resolution-sensitive, non-dimensional function (denoted as C^*). The coefficient C_{k2}^* (named by analogy to $C_{\varepsilon 2}$) is added to Eq. (10a) in comparison with Eq. (8) and, therefore, must be equal to one for SKE or wherever an HRL is meant to produce a strictly URANS solution. Wherever C_{k2}^* is non-unity, we take special care to note that ε_m must be regarded as a generalized scale-determining variable and not the actual quantitative rate of dissipation of k_m , which becomes $C_{k2}^* \varepsilon_m$.

In the following subsections, we present thirteen distinct HRL models divided into three categories as PANS-like (models using only a nonstandard C_{k2}^* coefficient), DES-like (i.e., models that include a non-unity C_{k2}^* coefficient, among others), or FSM-like (models using only a nonstandard C_μ^* coefficient). Three models, collectively known as continuous eddy simulation (CES) models, are categorized simultaneously as both DES and PANS-like—despite utilizing different sets of hybridized coefficients—due to their shared theoretical development and posterior performance. A concise listing of each HRL model to be presented is given in Table II.

A. PANS-like models

The partially averaged Navier–Stokes (PANS) modeling strategy, also known as the partially integrated transport model (PITM) strategy, is the modification of the $C_{\varepsilon 2}$ coefficient in the ε_m transport equation by a resolution control parameter, $R \in [0, 1]$, such that

$$C_{\varepsilon 2}^* = C_{\varepsilon 1} + R(C_{\varepsilon 2} - C_{\varepsilon 1}), \quad (11)$$

where $C_{\varepsilon 1}$ and $C_{\varepsilon 2}$ are the baseline SKE model constants. The PANS model of Girimaji¹⁷ is derived in physical space by making some broad assumptions about the relationship between the URANS transport equations for k_m - ε_m and the average of the modeled transport equations for k_m - ε_m , resulting in $R_{\text{pans}} = F_k / F_\varepsilon$, where $F_k = \mathcal{K}_m / \mathcal{K}_t$ and $F_\varepsilon = \mathcal{E}_m / \mathcal{E}_t$. The derivation requires the assumption that F_k and F_ε are constant in time. Additionally, in practice, it is assumed that the Reynolds number is high enough that $F_\varepsilon \approx 1$ for all desired grid resolutions. Furthermore, since F_k may be difficult to compute in complex flow geometries lacking homogeneity or stationarity, Girimaji and Abdol-Hamid¹⁶ used simple dimensional analysis to determine a lower bound for F_k and recommend that the user manually pick a temporally constant “target” resolution, R_c , for the simulation, with the recommendation that $R_c \sim (\Delta / \mathcal{L}_t)^{2/3}$, where $\mathcal{L}_t = \mathcal{K}_t^{3/2} / \mathcal{E}_t$ is the integral length scale.

The PITM^{18,29} formulation is derived in spectral space by assuming homogeneous turbulence, equilibrium inertial range dynamics,

TABLE I. Standard k - ε (SKE) and k -SGS model coefficients.

C_μ	σ_k	σ_ε	$C_{\varepsilon 1}$	$C_{\varepsilon 2}$	C_Δ	C_m	C_ε
0.09	1.0	1.3	1.44	1.714	0.61	$C_\mu C_\Delta$	$1/C_\Delta$

TABLE II. Summary of turbulence models to be tested, including abbreviated nomenclature, citations for model origins, and a basic definition of nonstandard model coefficients.

Type	Short name	Nonstandard C^*	Description
LES	k -SGS	N/A	One-equation model with constant coefficients ²⁵
RANS	SKE	N/A	Standard k - ϵ with $C_{\epsilon 2}$ tuned to decay rate ²⁶ .
	DES	C_{k2}^* [Eq. (13)]	“Standard” detached-eddy simulation ³⁰
DES-like	XLES	C_{k2}^*, C_{μ}^* [Eq. (14)]	extra-Large-Eddy simulation ³² or “Uni-LES” ³³
	RG- τ	$C_{k2}^*, C_{\mu}^*, C_{\epsilon 1}^*$, and $C_{\epsilon 2}^*$ [Eq. (15)]	Approximate renormalization-group model ³⁴
PANS-like	PANS- R_c	$C_{\epsilon 2}^*$ [Eq. (11); $R_c = F_{k,0}$]	Standard-practice PANS ¹⁶
	PANS- F_k/F_{ϵ}	$C_{\epsilon 2}^*$ [Eq. (11); $R = F_k/F_{\epsilon}$]	Theory-based PANS ¹⁷
	PITM	$C_{\epsilon 2}^*$ [Eqs. (11) and (12); $R = R_{vK}$]	Standard-practice PITM ¹⁹
DES- & PANS-like	CES-K	C_{k2}^* [Eqs. (18) and (12)]	DES-like CES ³⁶
	CES- X^a	C_{k2}^*, C_{μ}^* [Eqs. 12 and (20)]	XLES-like CES
	CES-S	$C_{\epsilon 2}^*$ [Eqs. (12) and (17)]	Standard-practice PANS-like CES ³⁶
FSM-like	FSM-Speziale	C_{μ}^* [Eq. (21)]	Standard-practice FSM due to Speziale ²⁰
	FSM-Dynamic ^a	C_{μ}^* [Eq. (22)]	Dynamic coefficient via Germano–Lilly procedure ⁴⁰
	FSM- R_{vK}^a	C_{μ}^* [Eq. (12); $F_{\mu} = R_{vK}$]	Tests $F_{\mu} = F_k$ ^{38,39} using R_{vK} estimate
	FSM- f_{Δ}	C_{μ}^* [Eq. (13)]	Tests C_{μ}^* component of XLES ⁴¹

^aSpecific model form is novel to this study.

and high Reynolds number (i.e., $F_{\epsilon} \approx 1$) from the start, resulting in $R_{pitm} = F_k$. In practice, Chaouat and Schiestel¹⁹ derive a target resolution parameter from a von Kármán type energy spectrum. While the von Kármán spectrum is a continuous class of spectra depending on the choice of a free exponent parameter, the standard choice (see source) results in

$$R_{vK} = \left[1 + C_0^{9/2} \left(\pi \frac{\mathcal{L}_t}{\Delta} \right)^3 \right]^{-2/9}, \quad (12)$$

where $C_0 = \frac{2}{3} C_K^{-1}$ and $C_K \approx 1.6$ is the Kolmogorov constant.

B. DES-like models

Detached eddy simulation (DES), as a modeling strategy, is the modification of one or more RANS model terms by substituting an LES model length scale in place of the RANS model length scale in order to achieve LES-like behavior from the model wherever the LES scale is smaller than the RANS scale.^{10,15} While DES was initially developed to address wall-bounded flows, as stated in Sec. I, this is still a unified model that is applicable to any turbulence flow configuration, wall-bounded or free, and including flows that lack a definable statistical average flow field. Since DES-type models have seen numerous applications in all types of practical turbulent flows, these are considered in our comprehensive model comparisons.

The standard form of DES—by far the most commonly used HRL model—modifies the implicit length scale in the destruction term of k_m (two-equation DES³⁰) or ν_m (one-equation DES¹) and nowhere else,

$$\text{DES: } C_{k2}^* = f_{\Delta}^{-1}, \quad f_{\Delta} = \min \left(1, \frac{C_{\Delta} \Delta}{\ell_m} \right), \quad (13)$$

where $C_{\Delta} = 0.61$, $\ell_m = k_m^{3/2} / \epsilon_m$, and all other SKE coefficients remain unmodified. For homogeneous turbulence with uniform structured grids, there is no difference between standard DES and any of its more sophisticated versions, such as delayed DES (DDDES) and improved delayed DES (IDDES). When $C_{\Delta} \Delta / \ell_m > 1$, f_{Δ} is limited down to 1, and DES reverts to the SKE RANS model at that grid point (though the simulation as a whole may not be considered a URANS). Wherever $f_{\Delta} < 1$, the model gives $C_{k2}^* \epsilon_m = k_m^{3/2} / (C_{\Delta} \Delta)$, which would be the same as the k -SGS LES model, except DES still uses ϵ_m to scale ν_m , and therefore, the simulation never actually reduces to k -SGS LES at any time or location.

In contrast, extra-large eddy simulation (XLES) does provide a complete reduction of a two-equation hybrid RANS form to k -SGS LES, in the limit where $f_{\Delta} < 1$ at all grid points, by modifying both C_{μ}^* and C_{k2}^* . XLES was first proposed by Bush and Mani,³¹ more widely popularized (and named) by Kok *et al.*,³² and re-derived from basic principles by Heinz,³³ in which the model is referred to as Unified LES-RANS, or Uni-LES, for short. For homogeneous turbulence simulated using k - ϵ , the XLES model can be given simply as

$$\text{XLES: } C_{\mu}^* = f_{\Delta} C_{\mu}, \quad C_{k2}^* = f_{\Delta}^{-1}, \quad (14)$$

where $C_{\Delta} = 0.61$, as in standard DES, and C_{μ} is the baseline SKE model constant.

A conceptually similar model that modifies all four C^* coefficients given in Eq. (10) is the approximate renormalization group (RG) derivation from De Langhe *et al.*³⁴ and De Langhe *et al.*,³⁵ which results in the alteration of the RANS timescale in both the k_m and ϵ_m equations, while ν_m is modified with a $\Delta^{4/3}$ scaling, consistent with Kolmogorov scaling arguments. The authors never named their model, so we label it RG- τ ,

$$\text{RG-}\tau: C_\mu^* = f_\Delta^{4/3} C_\mu, \quad C_{k2}^* = \frac{C_{e1}^*}{C_{e1}} = \frac{C_{e2}^*}{C_{e2}} = f_\Delta^{-2/3}, \quad (15)$$

where C_μ , C_{e1} , and C_{e2} are the baseline SKE model constants. The derivation does not recover the k -SGS model in the LES limit, instead RG- τ recovers a unique one-equation LES model based on the modified ε_m transport equation,

$$\frac{\partial \varepsilon_m}{\partial t} + \bar{u}_j \frac{\partial \varepsilon_m}{\partial x_j} = C_1^* \varepsilon_m^{2/3} - C_2^* \varepsilon_m^{4/3} + \frac{\partial}{\partial x_j} \left[\left(\nu + \frac{\nu_m}{\sigma_\varepsilon} \right) \frac{\partial \varepsilon_m}{\partial x_j} \right], \quad (16)$$

where $\nu_m = C_\mu (C_\Delta \Delta)^{4/3} \varepsilon_m^{1/3}$, $C_1^* = C_{e1} C_\mu (C_\Delta \Delta)^{2/3}$, and $C_2^* = C_{e2} (C_\Delta \Delta)^{-2/3}$. It should be noted that even though RG- τ does not require k_m in the LES limit, the transported k_m solution using Eqs. (10a) and (15) remains a consistent model form for the SGS kinetic energy.

The critical similarity of these three DES-like models is that they render the modeled viscous dissipation distinct from the scale-determining variable via a non-unity C_{k2}^* and behave distinctly as either RANS or LES in different regions of a homogeneous flow based on a local and instantaneous turbulence resolution parameter, f_Δ . In contrast, two additional DES-like models, which are described later in Sec. II C, use an averaged bridging-model style C_{k2}^* coefficient to similar effect without having a distinct LES mode.

C. PANS-like and DES-like CES models

The continuous eddy simulation (CES) paradigm of Heinz³⁶ is to take an existing hybridization approach, specifically DES, Uni-LES (a.k.a. XLES), and PITM, and then determine new global model coefficient(s) by a variational analysis to form a variable-resolution bridging model alternative in the case of DES and Uni-LES, and an improved resolution coefficient in the case of PITM. All CES models forms are meant to provide superior scale-resolving *self-consistency*²⁴ in the control of energy partitioning. The end result for PITM, which Heinz³⁶ classifies as ‘‘CES modification of the k - ε equations via the scale-determining equation,’’ or CES-KES, and which we shorten to CES-S, finds that the resolution control parameter of Eq. (11) should be $F_L^2 = F_k^3 / F_\varepsilon^2$, where $F_L = \mathcal{L}_m / \mathcal{L}_t$ and $\mathcal{L}_m = \mathcal{K}_m^{3/2} / \mathcal{E}_m$. However, the analysis presumes a high Re and coarse resolution where $F_\varepsilon \approx 1$. Moreover, F_k should always approach zero faster than F_ε as the resolution is increased. Therefore, in practice, F_L^2 is replaced by the approximate target value $R_{ces} = R_{vK}^3$, consistent with the approximation made in PITM such that the CES-S model is given as

$$\text{CES-S: } C_{e2}^* = C_{e1} + R_{vK}^3 (C_{e2} - C_{e1}). \quad (17)$$

The CES version of DES, which was originally named CES-KEK and we label as CES-K, was found by variational analysis to be

$$\text{CES-K: } C_{k2}^* = \gamma - R_{vK}^3 (\gamma - 1), \quad \gamma = \frac{C_{e2}}{C_{e1}}, \quad (18)$$

while the CES version of XLES (aka Uni-LES), originally named CES-KEKU and we label as CES-U, was found to be

$$\text{CES-U: } C_{k2}^* = [\gamma - R_{vK}^3 (\gamma - 1)]^{1/2}, \quad C_\mu^* = \frac{C_\mu}{C_{k2}^*}. \quad (19)$$

These definitions imply that CES-K and CES-U differ by a power of two in their respective C_{k2}^* formulas, which is different than the relationship between DES and XLES. It will be shown later in Appendix A that CES-U has noticeably lower accuracy at intermediate filter widths as compared to CES-K or CES-S. As such, we instead adopt a straightforward alternative form, which does have the same accuracy as CES-K and CES-S, which we label as CES-X,

$$\text{CES-X: } C_{k2}^* = \gamma - R_{vK}^3 (\gamma - 1), \quad C_\mu^* = \frac{C_\mu}{C_{k2}^*}. \quad (20)$$

D. FSM-like models

The original FSM variant is due to Speziale²⁰ and seeks to reduce the eddy viscosity by setting $C_\mu^* = F_\mu C_\mu$, where F_μ is an *ad hoc* function based on the filter scale, Δ , and Kolmogorov scale, $\eta = (\nu^3 / \mathcal{E}_t)$,

$$F_\mu = \left[1 - \exp\left(-\beta \frac{\Delta}{\eta}\right) \right]^\alpha. \quad (21)$$

Typically $\alpha = 1$ and here we set $\beta = 0.008$. Speziale’s original concept, which he termed VLES, was to solve for the RANS stress by averaging the resolved velocity field, but follow-on work from his collaborators,²¹ which coined the name FSM, re-interpreted the model to use the un-averaged velocity field in the model equations. Many variations on the definition of F_μ exist in the literature, often with their own unique names, such as limited numerical scales (LNS)³⁷ or partially resolved Navier–Stokes (PRNS).^{38,39}

It is also possible to formulate dynamic coefficient forms of FSM, as various dynamic-coefficient concepts are common in previous derivations of various HRL model types including both FSM⁴² and blended RANS-LES.^{43,44} For FSM, it is possible to compute a dynamic coefficient via the Germano–Lilly procedure,⁴⁰

$$C_\mu^* = \frac{\langle L_{ij} M_{ij} \rangle}{2 \langle M_{pq} M_{pq} \rangle}, \quad (22)$$

where a test filter is used to compute

$$\begin{aligned} L_{ij} &= \widetilde{\widetilde{u}_i u_j} - \widetilde{u}_i \widetilde{u}_j, & M_{ij} &= \widetilde{T_{ij}^m} - T_{ij}^{\text{test}}, \\ T_{ij}^m &= \frac{k_m^2}{\varepsilon_m} \widetilde{S}_{ij}, & T_{ij}^{\text{test}} &= \frac{k_{\text{test}}^2}{\varepsilon_{\text{test}}} \widetilde{S}_{ij}, \\ k_{\text{test}} &= \widetilde{k}_m + \frac{1}{2} \mathcal{L}_{ii}, & \varepsilon_{\text{test}} &= \widetilde{\varepsilon}_m + \nu \left(|\widetilde{S}|^2 - |\widetilde{S}|^2 \right). \end{aligned}$$

A more straightforward alternate choice to Speziale’s exponential form is $F_\mu = F_k$, which is found by comparing the trace of the modeled SGS stress tensor to the trace of the total Reynolds stress. This is the logic followed by the PRNS models, where rather idiosyncratic target estimates for F_k are formulated. Since one form of PITM and all forms of CES already use the same von Kármán spectrum estimate for F_k , a useful comparison can be made by setting $F_\mu = R_{vK}$. Another straightforward alternative uses $F_\mu = f_\Delta$, as in Johansen *et al.*,⁴¹ but also LNS³⁷ when the chosen RANS and LES models are SKE and k -SGS. This choice provides a useful counter-examples to DES and XLES and is also an example of using a localized resolution parameter instead of a global parameter.

E. Nonlinear feedback analysis of energy partitioning

Because of the power-law decay rate, the mean resolved and modeled energy can decrease by multiple orders of magnitude over time, depending on the filter scale. As such, there is a strong potential for large relative errors to accumulate at later times compared to the filtered DNS ground truth, even though these errors would be very small in absolute terms. Nevertheless, we need to be able to accurately evaluate the energy partitioning dynamics of each HRL model at all times and filter scales, irrespective of the differences in absolute magnitude. Therefore, we derive spatially averaged, non-dimensional equations for the generalized k - ε system in the same manner as Eq. (5). The result is a set of nonlinear ODEs governing the instantaneous power-law decay rates of \mathcal{K}_r , \mathcal{K}_m , and \mathcal{E}_m ,

$$\frac{d \ln \mathcal{K}_r}{d \ln t'} = -\frac{(t + n\tau_0)}{\mathcal{K}_r} (\langle \Pi_m \rangle + \mathcal{E}_r), \quad (23a)$$

$$\frac{d \ln \mathcal{K}_m}{d \ln t'} = \underbrace{\frac{(t + n\tau_0)}{\mathcal{K}_m} \langle C_\mu^* \frac{k_m^2}{\varepsilon_m} |\bar{S}|^2 \rangle}_{\mathcal{P}_K} - \underbrace{\frac{(t + n\tau_0)}{\mathcal{K}_m} \langle C_{k2}^* \varepsilon_m \rangle}_{\mathcal{D}_K}, \quad (23b)$$

$$\frac{d \ln \mathcal{E}_m}{d \ln t'} = \underbrace{\frac{(t + n\tau_0)}{\mathcal{E}_m} \langle C_{\varepsilon 1}^* C_\mu^* k_m |\bar{S}|^2 \rangle}_{\mathcal{P}_\varepsilon} - \underbrace{\frac{(t + n\tau_0)}{\mathcal{E}_m} \langle C_{\varepsilon 2}^* \frac{\varepsilon_m^2}{k_m} \rangle}_{\mathcal{D}_\varepsilon}. \quad (23c)$$

The right-hand side of each equation above can be set equal to a power-law exponent, as in Eq. (5), but one that is allowed to vary with time. In this way, the production \mathcal{P} and destruction \mathcal{D} terms of the modeled energy and dissipation represent strictly positive or negative contributions, respectively, to the slope of \mathcal{K}_m and \mathcal{E}_m plotted on log-log axes.

We can conveniently decompose \mathcal{D}_K by defining a dissipation-weighted mean C_{k2}^* coefficient, $\{C_{k2}^*\} = \langle C_{k2}^* \varepsilon_m \rangle / \mathcal{E}_m$ and approximate the remaining production and destruction terms by their leading-order Taylor-series expansions to remove statistical cross-correlations,

$$\mathcal{P}_K \approx (t + n\tau_0) \langle C_\mu^* \rangle \langle |\bar{S}|^2 \rangle \frac{\mathcal{K}_m}{\mathcal{E}_m}, \quad (24a)$$

$$\mathcal{P}_\varepsilon \approx (t + n\tau_0) \langle C_{\varepsilon 1}^* \rangle \langle C_\mu^* \rangle \langle |\bar{S}|^2 \rangle \frac{\mathcal{K}_m}{\mathcal{E}_m}, \quad (24b)$$

$$\mathcal{D}_K = (t + n\tau_0) \{C_{k2}^*\} \frac{\mathcal{E}_m}{\mathcal{K}_m}, \quad (24c)$$

$$\mathcal{D}_\varepsilon \approx (t + n\tau_0) \langle C_{\varepsilon 2}^* \rangle \frac{\mathcal{E}_m}{\mathcal{K}_m}. \quad (24d)$$

From these expansions, we can see clearly that Eqs. (23b) and (23c) are likely to be dynamically similar, with differences in partitioning dynamics largely driven by the specific definitions of each HRL model's generalized k - ε coefficients, C^* . We also recall that $\mathcal{E}_r = \nu \langle |\bar{S}|^2 \rangle$ and note that

$$\frac{(t + n\tau_0)}{\mathcal{K}_r} \langle \Pi_m \rangle = \frac{\mathcal{K}_m}{\mathcal{K}_r} \mathcal{P}_K.$$

As such, we can interpret model-to-model variations in energy partitioning as different feedback mechanisms operating on the same low-dimensional dynamical system. Each model starts from the same initial

state but follows a different trajectory through the space of instantaneous power-law decay rates for \mathcal{K}_r , \mathcal{K}_m , and \mathcal{E}_m . This framework is similar to the dynamical system fixed-point analysis utilized by Israel⁸ and references therein. The primary difference here is that we do not approximate the full high-dimensional dynamics [i.e., Eqs. (6) and (10)] with a closed set of ODEs that form a solvable low-dimensional system. Instead, we directly solve the high-dimensional system (i.e., perform 3D simulations) and then rely on an unclosed set of ODEs that approximate a low-dimensional dynamical system to simplify our interpretation and understanding of the high-dimensional results.

III. NUMERICAL METHODS

The physical configuration of the simulations is a triply-periodic cubic domain of size $2\pi \times 2\pi \times 2\pi$ and kinematic viscosity $\nu = 2.4414 \times 10^{-4}$. Equation (1) (DNS) or Eq. (6) with the relevant additional model transport equations (LES, SKE, and HRL) is solved on a uniform mesh using a pseudo-spectral solver. The solver is based on the open-source python package `shenfun`⁴⁵ and a simplified Navier–Stokes solver provided as part of the `spectralDNS` project.⁴⁶ We chose to use a pseudo-spectral solver for all simulations, including HRL simulations, in order to have explicit, spectral-space control over all numerical errors that might influence model behavior. All simulations utilized 2/3 rds truncation dealiasing, classical fourth-order Runge–Kutta explicit time integration, and dynamic time step-sizing based on the Courant–Freidrichs–Lewy (CFL) condition. Details of the code development can be found in [Appendix B](#).

A. Details of the direct numerical simulation

Conducting DNS of decaying HIT requires special consideration to achieve a power-law decay process,^{47,48} which is not a guaranteed outcome at early times due to the nature of performing simulations on a triply-periodic cube. Additionally, since a relatively long time series of DNS data are required for analysis, and as the turbulence decays it becomes increasingly well-resolved on a fixed mesh, we took advantage of the extreme simplicity of truncating and padding spectral-space checkpoint solution fields using `shenfun` in order to perform the DNS at different mesh resolutions over time, which decreased overall computational cost significantly.

The DNS run was initialized using a random initial velocity field with a prescribed isotropic energy spectrum on a 768^3 physical-domain mesh (giving a dealiasing cutoff wavenumber of $\kappa_c = 256$). Turbulence was sustained using bandpass linear forcing⁴⁹ of wavenumber shells $4 \leq \kappa \leq 6$ with a constant rate of energy injection $\varepsilon_{inj} = 1.0$ until \mathcal{K}_t and \mathcal{E}_t reached a statistically stationary state. At this point, the simulation was restarted on a 1536^3 physical-domain mesh ($\kappa_c = 512$) and evolved for an additional two integral time scales. The simulation was then restarted again at a final resolution of 2048^3 ($\kappa_c = 682$) and evolved until statistical stationarity was recovered (roughly one additional integral time), where the Kolmogorov scale resolution was $\kappa_c \eta = 1.33$. This point in the simulation is referred to as the *equilibrium* condition for the forced turbulence, which defines the (equilibrium) integral timescale of the forced turbulence, $\tau_{eq} = \mathcal{K}_{t,eq} / \mathcal{E}_{t,eq} = 1.125$. Forcing was then turned off, and the turbulence was allowed to decay for two full equilibrium integral time scales in order to asymptotically relax to a power-law decay process, at which point $\kappa_c \eta = 2.48$, providing extremely well-resolved viscous dissipation statistics.⁵⁰

TABLE III. DNS configuration and decaying HIT parameters.

	$t = -2\tau_{\text{eq}}$	$t = 0$ ($t' = 1$)	$t = 38\tau_{\text{eq}}$ ($t' = 19$)	
N_x		2048		Maximum physical mesh size
κ_c		682		Maximum spectral resolution
ν		2.441×10^{-4}		Kinematic viscosity
τ_{eq}		1.125		Integral timescale at $t = -2\tau_{\text{eq}}$
τ_0		1.693		Integral timescale at $t = 0$
$\kappa_c \eta$	1.33	2.48	5.44	Kolmogorov-scale resolution
Re_λ	186	80	45	Taylor-scale Reynolds number
\mathcal{K}_t	1.127	0.1383	2.295×10^{-3}	Total kinetic energy
\mathcal{E}_t	1.002	0.08171	7.138×10^{-5}	Total dissipation

The full 3D solution field output at this time we designate as $t = 0$, which is equivalent to $t' = 1$. This output was subsequently used to generate filtered and sub-sampled solution fields to be used as initial conditions for the HRL simulations. In order to continue collecting long-time statistics and 3D snapshots for post-processing, the DNS run was once again restarted, now at a lower mesh resolution of 1536^3 , and allowed to evolve for approximately seven τ_{eq} , at which point the DNS run was restarted one final time, at a resolution of 768^3 , and continued until $t = 38\tau_{\text{eq}}$.

Table III lists all the relevant numerical and dynamical parameters of the DNS data, including Taylor-scale Reynolds numbers Re_λ at the forced turbulence equilibrium state, and the initial and final decay states. Figure 1 shows the evolution of the Kolmogorov-scale resolution, $\kappa_c \eta(t)$, starting from before the final mesh refinement and showing both mesh coarsenings, as well as the kinetic energy spectra, $\widehat{E}(\kappa)$, at the final equilibrium point of the forced turbulence and before each mesh coarsening during decay. Figure 2 shows the linear least squares fit of the decay exponent n to the DNS data starting from $t = 0$ as well as the analytical URANS solutions of Eqs. (2). This results in $n = 1.401$ and $C_{e2} = 1.714$.

B. Details of the hybrid RANS-LES simulations

Our choice to use a pseudospectral method required solving the transport equations of the LES, SKE, and HRL models [Eq. (8) or Eqs. (10a) and (10b)] using logarithmic solution variables (that is, $\ln k_m$ and $\ln \varepsilon_m$) to enforce strict non-negativity and improve stability.⁵¹ An additional growth/decay time step limiter based on the transported model variables is also included in the dynamic time step update, in addition to advection and diffusion limiters,

$$\delta t^{\text{new}} = \min(2\delta t^{\text{old}}, \delta t_{\text{adv}}, \delta t_{\text{diff}}, \delta t_{k\varepsilon}), \quad (25a)$$

$$\delta t_{\text{adv}} = C_{\text{adv}} \frac{\delta x}{\max(|u_1| + |u_2| + |u_3|)}, \quad (25b)$$

$$\delta t_{\text{diff}} = C_{\text{diff}} \frac{\delta x^2}{2[\nu + \max(\nu_m)]}, \quad (25c)$$

$$\delta t_{k\varepsilon} = C_{k\varepsilon} \min \left| \frac{y}{\partial y / \partial t} \right|, \quad \forall y \in \{k_m, \varepsilon_m\}, \quad (25d)$$

where the min/max functions in Eq. (25) refer to finding the spatial minimum or maximum over the entire 3D domain, and the effect of

$\delta t_{k\varepsilon}$ is to prevent k_m or ε_m from growing (or shrinking) by more than the multiple $C_{k\varepsilon}$ at any point in the domain. That is, if $C_{k\varepsilon} = 0.1$, then k_m and ε_m cannot change by more than 10% at any mesh point in a single time step. For all simulations, $C_{\text{adv}} = 0.9$ and $C_{\text{diff}} = 0.33$, while we set $C_{k\varepsilon} = \min(0.9, 0.01\kappa_f)$. This limited URANS ($\kappa_f = 1$) to

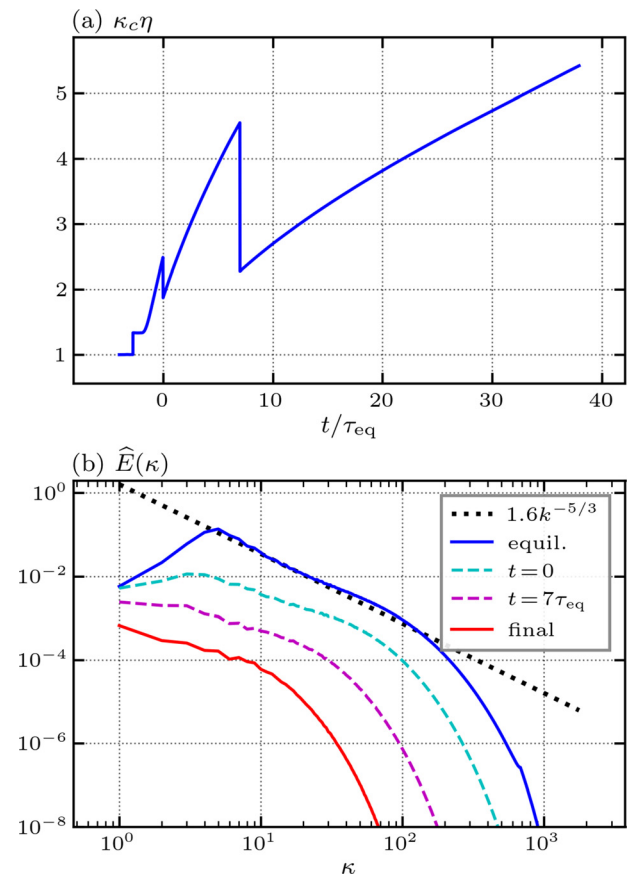


FIG. 1. Evolution of the DNS, (a) time series of the Kolmogorov-scale resolution, and (b) kinetic energy spectra at $t = -2\tau_{\text{eq}}$ (end of forcing), $t = 0$, $t = 7\tau_{\text{eq}}$ (mesh coarsening), and $t = 38\tau_{\text{eq}}$ (final output).

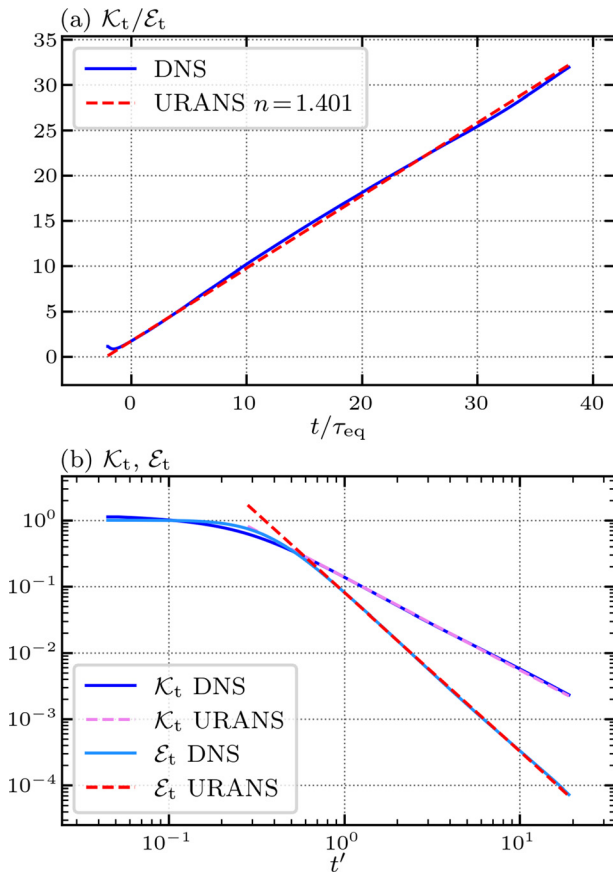


FIG. 2. Time series of (a) the integral timescale and (b) the total energy and dissipation showing a linear least squares fit of the decay exponent, n , and the URANS solution using the associated C_{i2} .

changes of 1% or less in k_m and ε_m , while allowing those variables to change by as much as 90% per time step at quasi-DNS resolution ($\kappa_f = 128$). The initial time step is set to a very small fixed number (10^{-8}) for all simulations, and the overall dynamic time step is allowed to double, at most, from one step to the next.

Convergence studies of the filter-to-grid width ratio, $\Delta/\delta x$, as well as tests of explicit right-hand side (RHS) Gaussian filtering were carried out for a subset of HRL models and filter wavenumbers, $\kappa_f = \pi/\Delta$, to determine the accuracy and computational cost of carrying out a systematic comparison of all of the HRL model variants, SKE, and LES. In addition, all models were run with standard 2/3 rds sharp spectral dealiasing at a resolution of $\Delta/\delta x = 3.0$ ($\kappa_c/\kappa_f = 2.0$) for $\kappa_f \leq 64$ without any additional stability enhancements. At $\kappa_f = 128$, simulations were run at a resolution of $\Delta/\delta x = 2.0$ with the additional stability provided by a secondary Gaussian filtering of the initial k_m and ε_m fields and explicit Gaussian filtering of both the eddy viscosity ν_m field and the non-conservative RHS terms. Further details of the switch to logarithmic solution variables, dealiasing, and the various configuration tests are provided in [Appendix B](#).

Initial conditions for the LES, SKE, and HRL simulations were computed from the DNS data output at the snapshot designated $t = 0$

TABLE IV. Coarse-grained physical-space mesh size, initial energy fraction, and initial dissipation fraction for the HRL simulations.

κ_f	N_x	$F_{k,0}$	$F_{\varepsilon,0}$
1	6	0.990	0.999 99
2	12	0.946	0.9998
4	24	0.825	0.998
8	48	0.642	0.991
16	96	0.451	0.965
32	192	0.273	0.877
64	384	0.131	0.660
128	512	0.0476	0.360

using a Gaussian filter to compute the resolved velocity \bar{u}_i , as well as k_m , and ε_m . These fields were then sub-sampled to form the coarse-grained initial conditions. [Table IV](#) provides a summary of the mesh sizes and initial F_k and F_ε values at $t = 0$ for each filter width of coarse-grained simulations. [Figure 3](#) shows filtered kinetic energy spectra of the DNS data at $t = 0$, as well as the time series of F_k and F_ε from filtered DNS data for each filter wavenumber $1 \leq \kappa_f \leq 128$.

The CES-K and CES-X models, having global non-unity C_{k2}^* values, can utilize two different initial conditions, based on the DNS-derived dissipation, to slightly different behavior. Denoting the correct initial subgrid-scale dissipation rate as ε_{sgs}^0 , the default condition (IC1) initializes $\varepsilon_m^0 = \varepsilon_{sgs}^0$, leading the initial modeled dissipation of k_m in [Eq. \(10a\)](#) to be greater than the filtered DNS field at all points, $C_{k2}^* \varepsilon_m^0 > \varepsilon_{sgs}^0$. The second initial condition (IC2) sets $\varepsilon_m^0 = \varepsilon_{sgs}^0 / C_{k2}^*$ such that the modeled dissipation of k_m is identical to the filtered DNS field at all points, $C_{k2}^* \varepsilon_m^0 \equiv \varepsilon_{sgs}^0$. It will be shown in [Sec. IV](#) that IC1 allows CES-K and CES-X to behave as DES-like while IC2 allows these models to behave as PANS-like, without any modification to the model forms themselves. To summarize, test results for all models except CES-K and CES-X are presented using only IC1, while test results for CES-K and CES-X are presented twice: once using IC1 to produce their expected DES-like behavior, and once using IC2 to produce a PANS-like behavior. DES-like models employing a spatially localized C_{k2}^* function—namely, standard DES, XLES, and RG- τ —produce essentially identical results using either IC1 or IC2 and cannot produce PANS-like behavior with a change in initial conditions, which we explain in detail in [Appendix C](#).

IV. RESULTS AND DISCUSSION

In this section, we present detailed results of the energy partitioning dynamics for each HRL model. Wherever DNS data are presented alongside SKE, HRL, and LES dynamics, it has been post-processed from fully resolved simulation outputs via Gaussian spatial filtering and constitutes the true SGS dynamics. That is, we directly compute the true turbulence stress τ_{ij} , cross-scale energy transfer Π , SGS kinetic energy k_m , and SGS viscous dissipation ε_m , for each filter scale κ_f , and at each DNS time output. However, we do not compute the true production and destruction terms for the temporal evolution of ε_m and, therefore, present DNS truth data for \mathcal{P}_K and \mathcal{D}_K , but not for \mathcal{P}_E and \mathcal{D}_E . Similarly, since the k -SGS model uses an algebraic formula for ε_m , we also do not model or compute \mathcal{P}_E and \mathcal{D}_E for the LES baseline.

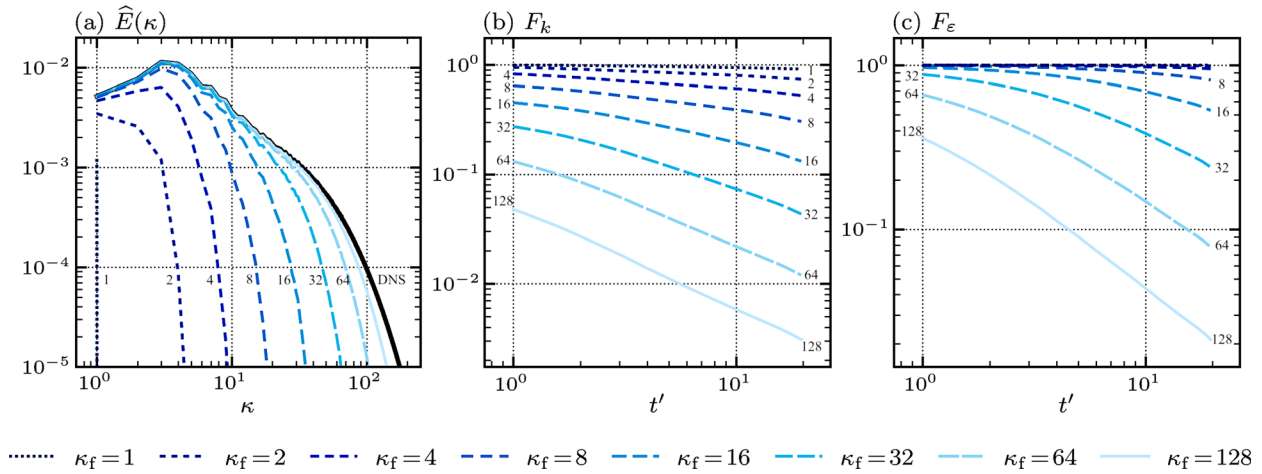


FIG. 3. (a) Filtered kinetic energy spectra at $t = 0$ from DNS, and time series of (b) F_k and (c) F_ϵ from filtered DNS data for each filter wavenumber $1 \leq \kappa_f \leq 128$.

Figure 4 provides an overview of how the standard-practice forms of PITM, DES, CES-S, and FSM perform in comparison with the SKE and k -SGS LES baselines and the filtered DNS ground truth, in time series of the spatially averaged resolved energy, \mathcal{K}_r , and modeled energy, \mathcal{K}_m , at every filter width. This provides a basic visualization of both how kinetic energy is partitioned, and how each partition decays in time, while comparing a representative variant of each model category. It can be seen in

Figure 4(a) that all of the HRL models, but not SKE, achieve a very accurate evolution of \mathcal{K}_r as resolution increases toward DNS. PITM, in particular, has excellent accuracy in \mathcal{K}_r across all scales $\kappa_f \geq 4$. In contrast, Speziale’s FSM is clearly the worst performing model for $\kappa_f \leq 8$, though no model compares well to DNS for $\kappa_f \leq 2$, except for the LES at $\kappa_f = 2$ by coincidence (we note that the LES dramatically undershoots the DNS truth for $\kappa_f = 1$ and then overshoots DNS for $\kappa_f = 4$).

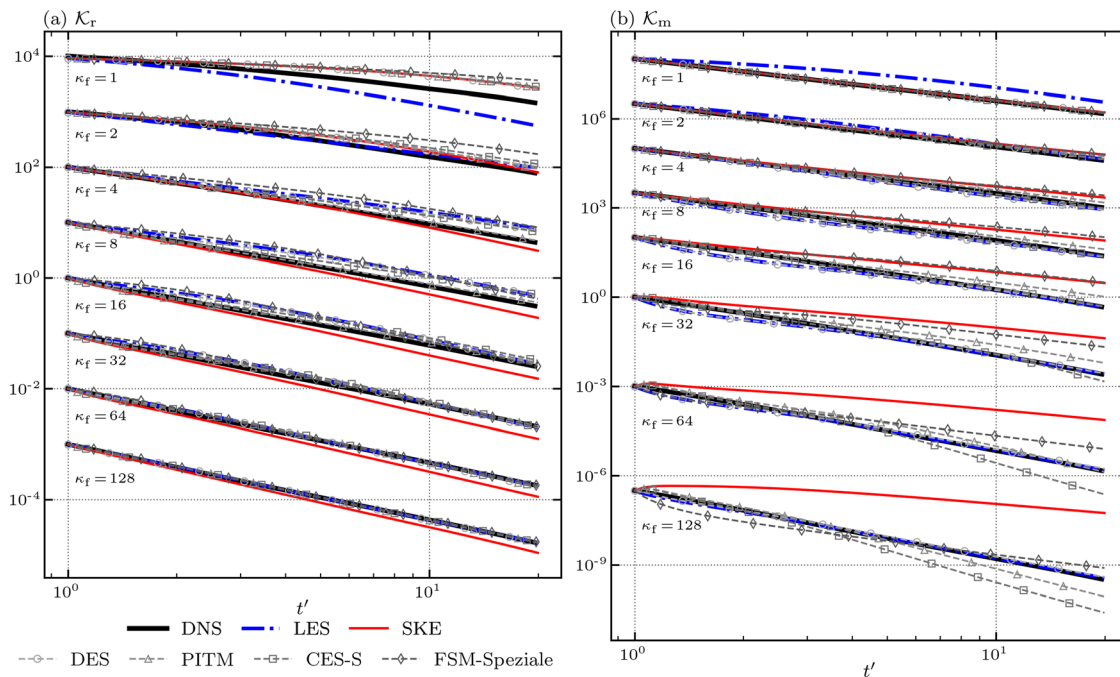


FIG. 4. Time series of (a) mean modeled kinetic energy, \mathcal{K}_m , and (b) mean resolved kinetic energy, \mathcal{K}_r for filtered DNS, k -SGS LES, SKE RANS, DES, PITM, CES-S, and FSM-Speziale. Values are normalized by the corresponding filtered DNS value at $t' = 1$ and then offset by a different fixed multiple for each κ_f to show each subplot on a single log-scaled vertical axis.

Turning to Fig. 4(b), only the LES and DES (which have a close mathematical relationship) show a high degree of accuracy in \mathcal{K}_m at fine resolutions ($\kappa_f \geq 16$) and later times ($t' > 3$). However, PITM and CES-S clearly outperform FSM for most filter scales ($2 \leq \kappa_f \leq 32$) and at early times at the finest filter scales ($\kappa_f \geq 64$). In fact, FSM notably performs worse than even SKE at late times ($t' > 5$) at the intermediate scale $\kappa_f = 8$, which, with $F_{k,0} \approx 2/3$ and $F_{e,0} \approx 1$, is precisely the kind of intermediate resolution at which an HRL model is most necessary as an alternative to RANS and LES. In contrast, PITM and CES-S both demonstrate highly inaccurate decay rates for \mathcal{K}_m at near-DNS resolution ($\kappa_f = 128$) and late times.

While these quantitative performance comparisons between models are an important aspect of the verification and validation (V&V) process, they do not provide any insight into why each model behaves as it does. For that, we turn to the novel nonlinear feedback analysis we derived in Sec. II E. Critical to this novel framework is whether or not the first-order truncations in Eqs. (24a), (24b), and (24d) can explain the relationship between each HRL's initial perturbation to, and subsequent deviations from, the baseline SKE dynamics. As previously stated, we did not attempt to derive a fully closed reduced-order approximation that could be used in place of full 3D CFD simulations, and therefore, it is sufficient that these approximations have low *a priori* error. We computed the root mean square (RMS) relative errors between \mathcal{P}_K , \mathcal{P}_E , and \mathcal{D}_E as defined in Eq. (23), and post-processed calculations of their approximations at each time from the simulation outputs of $\langle C^* \rangle$, $\langle |\bar{S}|^2 \rangle$, \mathcal{K}_m , and \mathcal{E}_m .

The SKE model, having no localized model coefficients (i.e., $\langle C^* \rangle = C$), generally had a lower relative error than any HRL model, with an RMS error ranging from 0.017% for \mathcal{D}_E at $\kappa_f = 1$, through intermediate errors such as 5.83% for \mathcal{P}_K at $\kappa_f = 16$, up to 14.9% for \mathcal{P}_E at $\kappa_f = 128$. In contrast, the RG- τ model—which has four localized general coefficients contributing to increased cross-correlations in higher-order terms—generally had the worst error rates, roughly 1.5 times higher than SKE, with its highest RMS error being 32.7%, also for \mathcal{P}_E at $\kappa_f = 128$. However, the most substantial differences between RG- τ (and indeed any model with a localized coefficient) and lower-error models with global coefficients are during a short window of time near $t' = 1$, which will be addressed later in this section. These results indicate that Eq. (24) can be employed to provide a plausible explanation of the nonlinear energy partitioning behavior.

In the following subsections, we evaluate the PANS-like models in fine detail first, as their uniform use of a single, global-valued, generalized coefficient to modify SKE is the simplest to analyze as a feedback mechanism operating on the simplified dynamical system implied by Eq. (24). We then evaluate the FSM-like models, which all use the single generalized C_μ^* coefficient. Three of these variants use a global-valued coefficient, which provides a counterexample to the PANS-like feedback mechanism. The fourth FSM model, FSM- f_Δ , uses the same local-valued C_μ^* coefficient as employed by k -SGS and XLES, providing a necessary foundation for the subsequent detailed evaluation of the DES-like models.

A. PANS-like models

In order to thoroughly test the dynamical behavior of the PANS-like model form, we evaluate six different variants, including the standard PANS practice of choosing a constant resolution control

parameter (RCP), R_c , the standard PITM RCP, R_{vK} , and a time-varying version of the theoretical RCP for PANS, $R = F_k/F_e$ (in which F_k and F_e represent the observed values of the HRL and not the filtered DNS), as well as the all three CES variants using R_{vK}^3 . Here, CES-K and CES-X start from initial condition option #2 (IC2) to induce PANS-like behavior.

Figure 5 shows the time evolution of the mean model dynamics of the six PANS-like models at $\kappa_f = 2, 16$, and 128. While there is a quantitative difference between PANS/PITM (shown in shades of purple) and CES (shades of orange), all six variants exhibit the same qualitative behavior at each filter scale. This is in spite of the fact that CES-K and CES-X use different generalized coefficients and a different initial condition for \mathcal{E}_m , which is highlighted in the zoom inset plot of Fig. 5(c). In fact, there is a very high degree of quantitative agreement between the three CES variants (see also Appendix A).

Figure 6 shows the detailed time evolution of the nonlinear power-law dynamics, as defined by Eq. (23), at $\kappa_f = 16$. Results at this filter width, which lies halfway between URANS and DNS, are demonstrative of PANS-like energy partitioning behavior at all κ_f . There are two important observations to be made from these data. The first is that there is a strong correlation between the two production terms, \mathcal{P}_K and \mathcal{P}_E [Figs. 16(e) and 16(h)], and between the two destruction terms, \mathcal{D}_K and \mathcal{D}_E [Figs. 16(f) and 16(i)], for all PANS-like models, lending additional credence to the approximations given in Eq. (24). The second is that all six PANS-like models exhibit the same feedback mechanism, with time series of each individual panel generally rising and falling together, even if by varying degrees. Indeed, there is significantly greater quantitative variation within the PANS/PITM models than between the CES models, with PANS- R_c showing the least deviation from the SKE baseline.

We recall that in four of the six variants (the two PANS, PITM, and CES-S), only C_{e2}^* is modified with respect to the SKE model, while the non-conforming CES-K and CES-X produce results very similar to CES-S at all times. Therefore, we conduct the following feedback analysis for all PANS-like variants using just the C_{e2}^* mechanism. The analysis starts with the perturbation to the initial value of \mathcal{D}_E , shown in the inset of Fig. 6(i), due to smaller values for C_{e2}^* as compared to SKE. This perturbation is also reflected as an initial increase in the logarithmic slope of \mathcal{E}_m in Fig. 6(g) compared to the SKE baseline (i.e., a slower decay rate).

The slower decay of \mathcal{E}_m in turn induces substantially more positive trends in \mathcal{D}_K and \mathcal{D}_E [panels (f) and (i)], which vary in proportion with \mathcal{E}_m , and, therefore, more negative trends in the logarithmic derivatives of \mathcal{K}_m and \mathcal{E}_m [panels (d) and (g)]. These trends lead to lower values for \mathcal{K}_m after $t' = 1$, while limiting the extent to which \mathcal{E}_m becomes inflated compared to SKE. The initial perturbation also induces a substantially more negative trend in $\langle \Pi_m \rangle / \mathcal{K}_r$ [panel (b)], which approximately varies inversely with \mathcal{E}_m . This is equivalently seen as a more positive trend in the derivative of \mathcal{K}_r [panel (a)] and, thus, larger \mathcal{K}_r after $t' = 1$.

By the same approximation, \mathcal{P}_K and \mathcal{P}_E should show the same decreasing trend as $\langle \Pi_m \rangle / \mathcal{K}_r$. Yet, these terms become only slightly more negative at early times. This difference at $t' = 1$ cannot be explained by our reduced-order system but would only have served to reinforce the changes to the power-law trends in panels (d) and (g). Once the feedback is established (i.e., for times $t' > 1$), however, we can attribute some of the difference between $\langle \Pi_m \rangle / \mathcal{K}_r$ and the \mathcal{P}

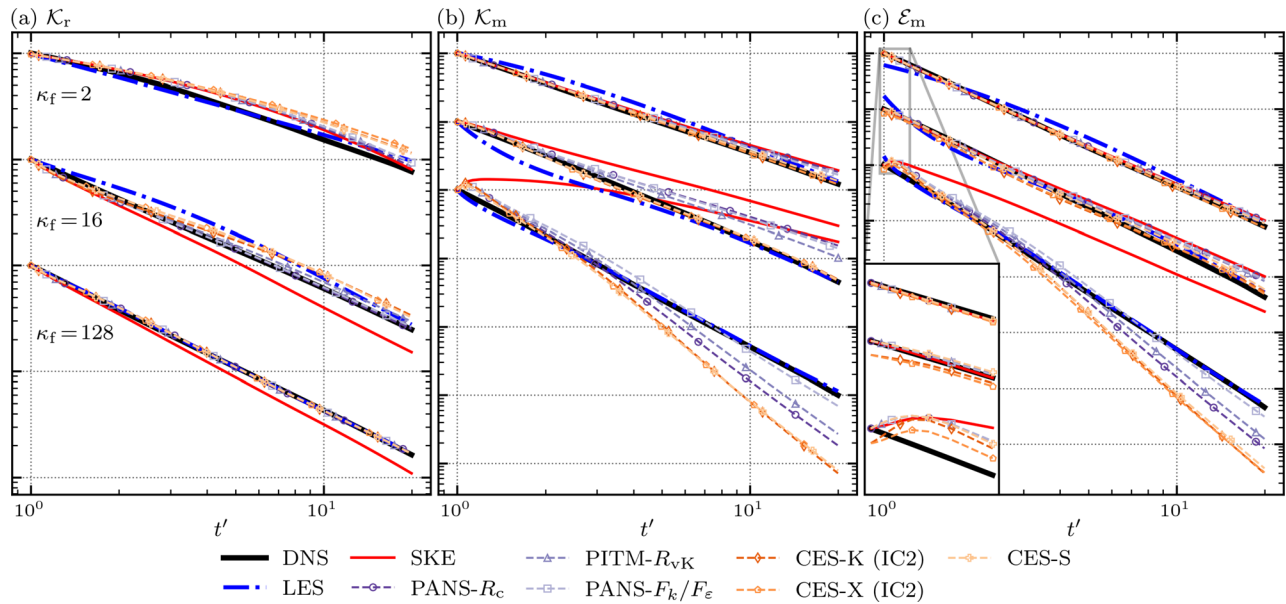


FIG. 5. Comparing the mean model dynamics of six PANS-like HRL variants at filter wavenumbers $\kappa_f = 2, 16$, and 128 . Initial condition option #2 (IC2) is used in the cases of CES-K and CES-X. Shown are time series of (a) mean resolved kinetic energy, \mathcal{K}_r , (b) mean modeled kinetic energy, \mathcal{K}_m , and (c) mean modeled dissipation, \mathcal{E}_m . Time series for all turbulence models are normalized by the corresponding filtered DNS value at $t' = 1$ and then offset by a different fixed multiple for each κ_f to show each subplot on a single log-scaled vertical axis.

terms to the fact that the leading-order approximation of the former is proportional to $\mathcal{K}_m^2/\mathcal{K}_r$, while the latter are only proportional to \mathcal{K}_m .

In any case, the increased magnitude of \mathcal{K}_r directly alters the ratio $\mathcal{E}_r/\mathcal{K}_r$ and likely indirectly inflates \mathcal{E}_r , as the power-law exponents of the resolved-scale energy and dissipation should be linearly dependent in the same manner as their subgrid-scale counterparts. This expected increase in $\mathcal{E}_r/\mathcal{K}_r$ can be seen to occur in panel (c) in less than one decay time (i.e., $t' < 2$). The increasing trend in \mathcal{E}_r is directly equivalent to an increasing trend in $\langle |\bar{S}|^2 \rangle$, which should reinforce the positive trends in $\mathcal{D}_\mathcal{K}$ and $\mathcal{D}_\mathcal{E}$, while counteracting the negative trends in $\mathcal{P}_\mathcal{K}$, $\mathcal{P}_\mathcal{E}$, and $\langle \Pi_m \rangle/\mathcal{K}_r$. Indeed, we see in panels (e) and (h) an immediate and strong reversal in $\mathcal{P}_\mathcal{K}$ and $\mathcal{P}_\mathcal{E}$ toward positive growth at this time, while $\langle \Pi_m \rangle/\mathcal{K}_r$ begins to flatten out. $\mathcal{D}_\mathcal{K}$ and $\mathcal{D}_\mathcal{E}$ show an acceleration in their positive feedback slightly later, just before $t' = 3$, while $d \ln \mathcal{K}_r / d \ln t'$ peaks at roughly the same time.

Over the long-term, the trends in each right-hand-side term of Eq. (23), except $\langle \Pi_m \rangle/\mathcal{K}_r$, remain essentially constant after $t' = 3$, and heading in the same direction as the DNS truth. On the other hand, the trends in the power-law exponents, as well as $\langle \Pi_m \rangle/\mathcal{K}_r$, slowly oscillate around more-or-less DNS-like trends over time. The overall net effect of this feedback mechanism is to cause PANS-like HRL models to rapidly deviate from their SKE starting point at early times and behave *qualitatively* similarly to the DNS truth over medium and long time scales, even while no individual PANS-like model quantitatively matches DNS for all quantities of interest.

The nonlinear feedback mechanism of the PANS-like models is essentially the same as that outlined above for all κ_f , though there are quantitative differences, which we elaborate at the near-URANS filter scale, $\kappa_f = 2$, and at the near-DNS filter scale, $\kappa_f = 128$. Starting with the near-URANS limit, Fig. 7 shows the detailed time evolution of the

nonlinear power-law dynamics for the PANS-like variants at $\kappa_f = 2$. Because of the strong dynamical similarity between production and destruction terms demonstrated previously, we show only the \mathcal{K}_m dynamics for brevity, and not the \mathcal{E}_m dynamics, which approximately match the \mathcal{K}_m results.

The same feedback mechanism is active at $\kappa_f = 2$ as at $\kappa_f = 16$, with the exception that the progression of the feedback is much slower, and quantitatively much less pronounced. Subsequent to the initial perturbation in $\mathcal{D}_\mathcal{E}$ and \mathcal{E}_m (which is not shown), we can follow the feedback mechanism starting from the more positive trend in $\mathcal{D}_\mathcal{K}$ [panel (f)] and a less positive trend in $\langle \Pi_m \rangle/\mathcal{K}_r$ immediately after $t' = 1$. These changes are equivalently seen as a less positive trend in the logarithmic derivative of \mathcal{K}_m [panel (d)] and a less negative trend in the derivative of \mathcal{K}_r [panel (a)].

As before, there are no substantive changes to $\mathcal{P}_\mathcal{K}$ [panel (e)] and $\mathcal{P}_\mathcal{E}$ (not shown) in comparison to SKE at early times. However, the positive trend in the logarithmic derivative of \mathcal{K}_r , which is only a very tiny change in the magnitude of \mathcal{K}_r (see Fig. 5), begins to induce a noticeable increase in $\mathcal{E}_r/\mathcal{K}_r$ (and therefore $\langle |\bar{S}|^2 \rangle$) after roughly $t' = 5$. Once this occurs, $\mathcal{P}_\mathcal{K}$ increases relative to SKE, while the already enhanced growth in $\mathcal{D}_\mathcal{K}$ accelerates further, and the reduced growth in $\langle \Pi_m \rangle/\mathcal{K}_r$ is partially counteracted. These trends remain in place for all later times, with the very-low-frequency oscillations seen in the power-law exponents at $\kappa_f = 16$ not directly apparent at $\kappa_f = 2$, likely due to the slower feedback progression and chosen cut-off time of the simulations.

In contrast, the feedback mechanism at $\kappa_f = 128$ proceeds much more quickly, as shown in Fig. 8, resulting in an extended period of late-time asymptotic behavior in the net decay rate of \mathcal{K}_m (and also \mathcal{E}_m) that is substantially different from SKE. The net decay rate of \mathcal{K}_r

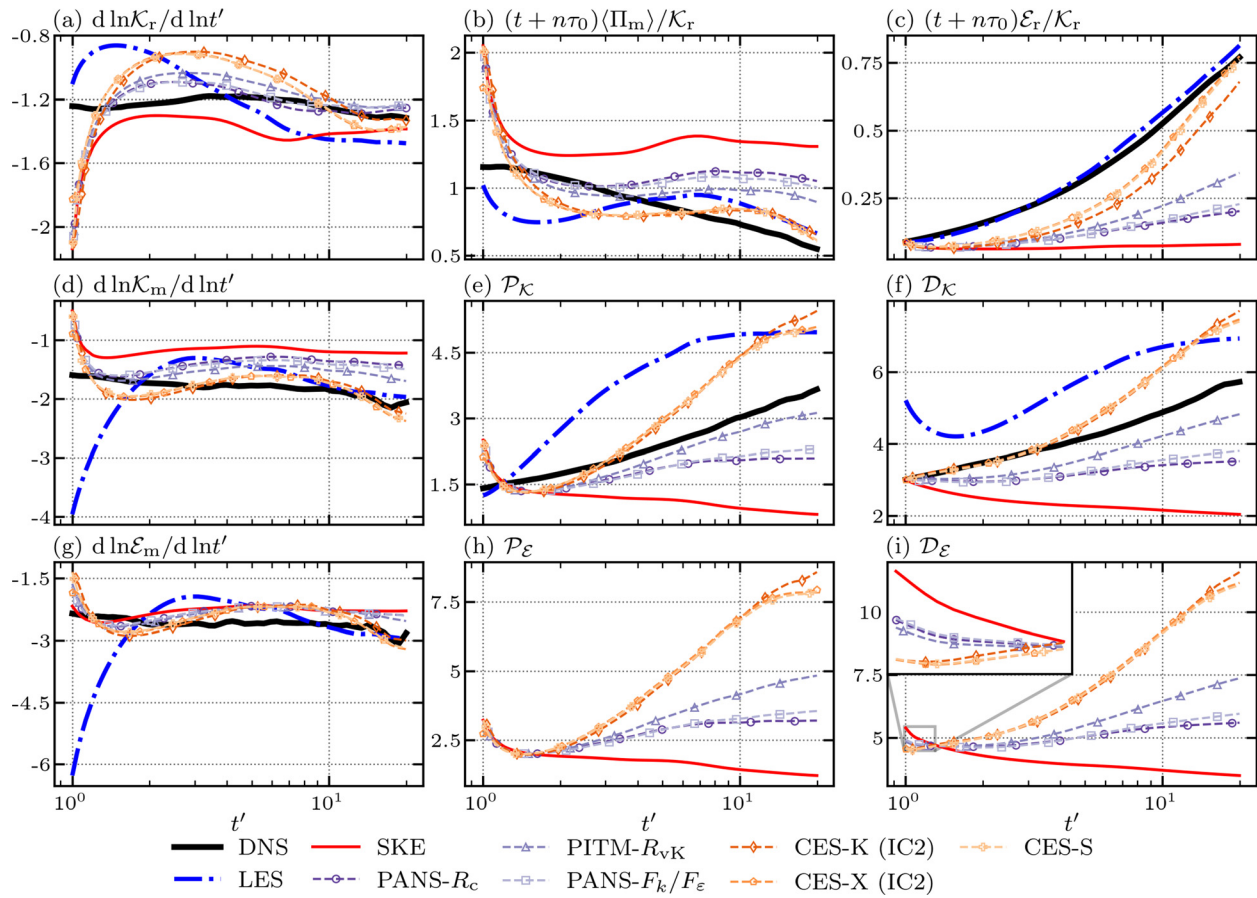


FIG. 6. Comparing the energy partitioning dynamics of six PANS-like HRL variants at filter wavenumber $\kappa_f = 16$. Initial condition option #2 (IC2) is used in the case of CES-K. Shown are time series of (first row) (a) the instantaneous power-law exponent of \mathcal{K}_r , (b) non-dimensional destruction of \mathcal{K}_r due to $\langle \Pi_m \rangle$, (c) non-dimensional destruction of \mathcal{K}_r due to \mathcal{E}_r ; (second row) (d) the instantaneous power-law exponent of \mathcal{K}_m , (e) non-dimensional production rate of \mathcal{K}_m , $\mathcal{P}_{\mathcal{K}}$, (f) non-dimensional destruction rate of \mathcal{K}_m , $\mathcal{D}_{\mathcal{K}}$; (third row) (g) the instantaneous power-law exponent of \mathcal{E}_m , (h) non-dimensional production rate of \mathcal{E}_m , $\mathcal{P}_{\mathcal{E}}$, and (i) non-dimensional destruction rate of \mathcal{E}_m , $\mathcal{D}_{\mathcal{E}}$.

and the individual production and destruction terms closely match the DNS truth at late times. However, the net decay rates of \mathcal{K}_m and \mathcal{E}_m undershoot the DNS truth, leading to the large discrepancies seen in Fig. 5 and in the $\langle \Pi_m \rangle / \mathcal{K}_r$ evolution [Fig. 8(b)].

These changes in behavior from $\kappa_f = 2$ to $\kappa_f = 128$ are a consistent trend across all κ_f . Quantitatively, there is also a clear trend that at coarser resolutions ($\kappa_f \leq 16$), the CES variants are more accurate than any PANS/PITM model, while at finer resolutions ($\kappa_f > 16$), the PANS- $R = F_k/F_\varepsilon$ variant notably outperforms the other five variants. This should not be a surprise, since the CES, PANS- R_c , and PITM formulas were derived under the assumption of high Reynolds number and coarse resolution (i.e., where $F_\varepsilon \approx 1$), neither of which is true in these cases, while the original PANS derivation does not make this assumption.

B. FSM-like models

The primary purposes in testing the FSM-like model form are to provide an alternate example of variable-resolution bridging from the PANS-like form and to discern the dynamical relevance of the

hybridized C_μ^* coefficient in the XLES, RG- τ , and CES-K models in comparison with DES and CES-X. As such, we analyze four different formulas for computing the eddy-viscosity reduction factor F_μ : (i) the original formula due to Speziale, (ii) a global Germano-Lilly dynamic procedure, (iii) the PITM/CES resolution parameter $F_\mu = R_{vK}$, and (iv) the XLES/ k -SGS reduction factor f_Δ . Of these, the Speziale coefficient and R_{vK} monotonically decrease from $F_\mu = 1$ (RANS) to $F_\mu = 0$ (DNS) as κ_f and time increase. In contrast, neither f_Δ nor the dynamic coefficient decrease monotonically with filter scale or time. In the latter case, the Germano-Lilly procedure is based on the assumption of κ_f being in a region of extended scale similarity, which does not exist for our DNS, as evidenced by Figs. 1(b) and 3(a). The behavior of f_Δ will be analyzed in detail in the next subsection. By testing both global and local coefficients, as well as bridging (i.e., monotonically decreasing) and non-bridging formulas, our evaluation of the FSM model form is quite robust.

Figure 9 shows the time evolution of the mean model dynamics of the FSM-like models, at $\kappa_f = 2, 16$, and 128. It can be seen that all four FSM variants demonstrate the same qualitative behavior as FSM-Speziale. In particular, all four variants show an increase in resolved

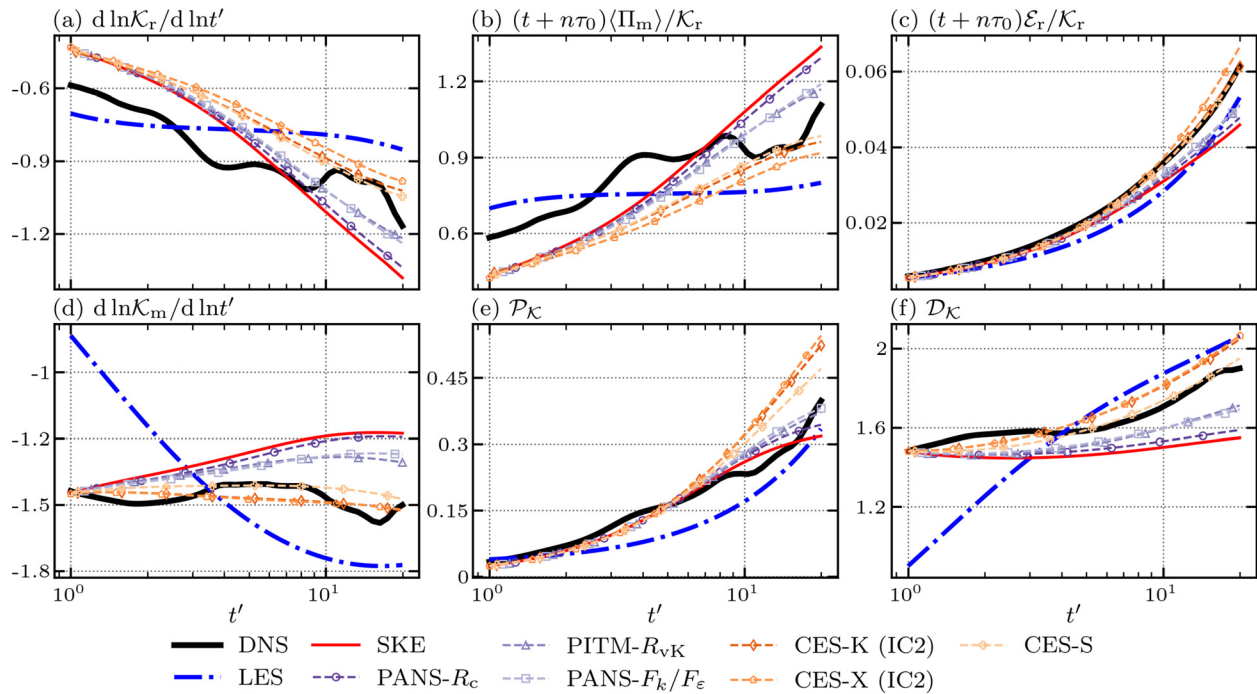


FIG. 7. Energy partitioning dynamics of standard-practice PANS, PITM, and CES-K, and theory-based CES-S at the near-URANS limit of $\kappa_f = 2$. Initial condition option #2 (IC2) is used in the case of CES-K. Shown are time series of (first row) (a) the instantaneous power-law exponent of \mathcal{K}_r , (b) non-dimensional destruction of \mathcal{K}_r due to $\langle \Pi_m \rangle$, (c) non-dimensional destruction of \mathcal{K}_r due to \mathcal{E}_r ; (second row) (d) the instantaneous power-law exponent of \mathcal{K}_m , and (e) non-dimensional production rate of \mathcal{K}_m , $\mathcal{P}_{\mathcal{K}}$.

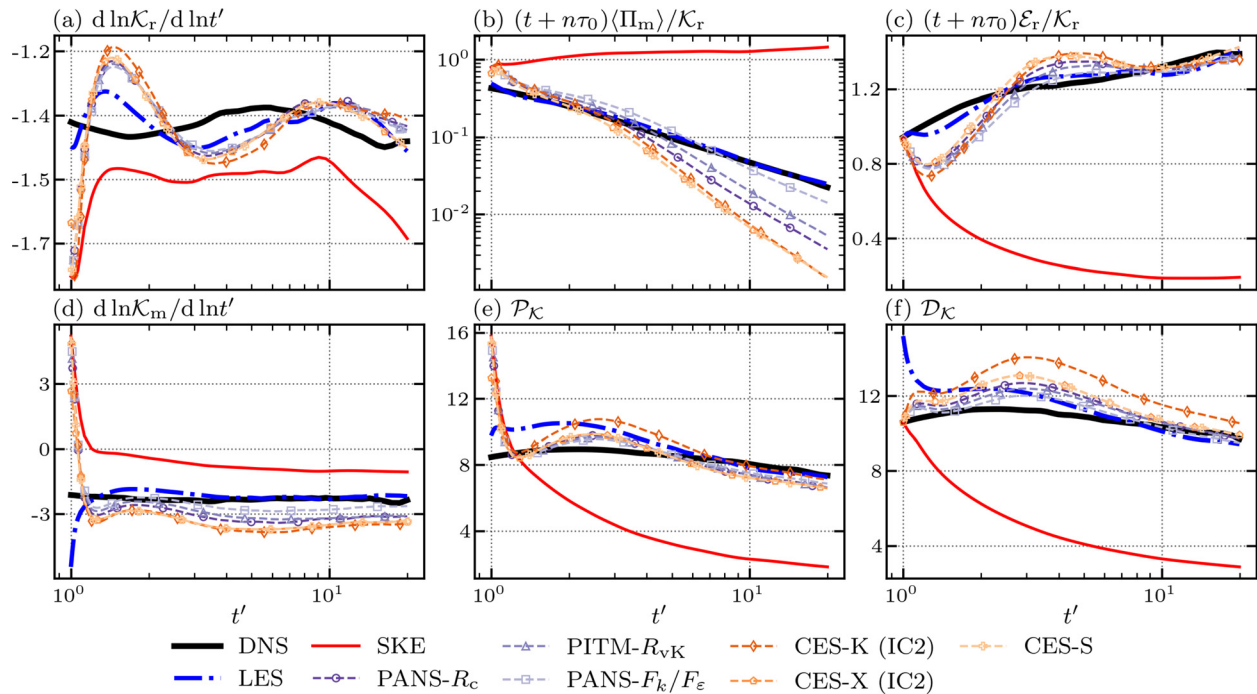


FIG. 8. Energy partitioning dynamics of the theory-based PANS, PITM, and CES-S, along with standard CES-K using IC2 at the near-DNS limit of $\kappa_f = 128$. Shown are time series of (first row) (a) the instantaneous power-law exponent of \mathcal{K}_r , (b) non-dimensional destruction of \mathcal{K}_r due to $\langle \Pi_m \rangle$, (c) non-dimensional destruction of \mathcal{K}_r due to \mathcal{E}_r ; (second row) (d) the instantaneous power-law exponent of \mathcal{K}_m , (e) non-dimensional production rate of \mathcal{K}_m , $\mathcal{P}_{\mathcal{K}}$.

07 October 2024 15:15:00

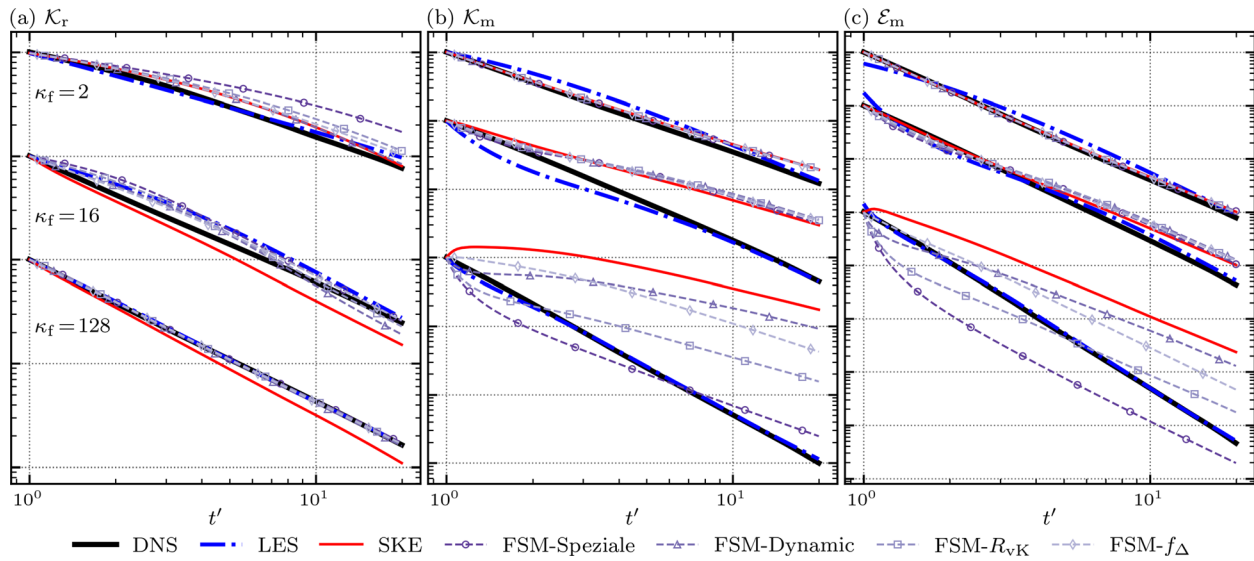


FIG. 9. Comparing the mean model dynamics of the four FSM-like variants at filter wavenumbers $\kappa_f = 2, 16,$ and $128.$ Shown are time series of (a) mean resolved kinetic energy, $\mathcal{K}_r,$ (b) mean modeled kinetic energy, $\mathcal{K}_m,$ and (c) mean modeled dissipation, $\mathcal{E}_m.$ Time series for all turbulence models are normalized by the corresponding filtered DNS value at $t = 0$ and then offset by a different fixed multiple for each κ_f and quantity of interest to show each subplot on a single vertical axis.

energy levels compared to SKE at all three resolutions [Fig. 9(a)], with a close agreement with DNS at the near-DNS resolution. If only these results were known, one might conclude that FSM significantly improves the ability of SKE to perform scale-resolving simulations beyond URANS. However, it is also immediately clear from panels (b) and (c) that the FSM models in fact do not show any improved self-consistency in modeling the subgrid-scale dynamics as compared to SKE. In fact, all four variants closely agree with SKE at $\kappa_f = 2$ and $16,$ and demonstrate the same qualitative trends as SKE at $\kappa_f = 128.$ To understand how FSM can behave so much differently than the PANS-like models or k -SGS LES, even while converging to DNS in the resolved energy, we turn to the detailed nonlinear power-law dynamics.

Figure 10 shows the detailed time evolution of these dynamics for the FSM-like variants at $\kappa_f = 16.$ It can be clearly seen that all four variants have a qualitatively similar dynamic behavior which is much different than the PANS feedback mechanism. Here, the FSM models start by reducing the initial values of $\langle \Pi_m \rangle / \mathcal{K}_r, \mathcal{P}_{\mathcal{K}},$ and $\mathcal{P}_{\mathcal{E}}$ [panels (b), (e), and (h)]. These perturbations induce an immediate relative increase in $\langle |\bar{S}|^2 \rangle,$ as given by $\mathcal{E}_r / \mathcal{K}_r$ [panel (c)] for essentially all times, and relative decreases in $\mathcal{D}_{\mathcal{K}}$ and $\mathcal{D}_{\mathcal{E}}$ [panels (f) and (i)] at the earliest times. The initial offsets in $\mathcal{P}_{\mathcal{K}}$ and $\mathcal{P}_{\mathcal{E}}$ and the initial decreased trends in $\mathcal{D}_{\mathcal{K}}$ and $\mathcal{D}_{\mathcal{E}}$ at very early times are revealed to induce nothing more than a damped oscillation about the SKE baseline over the full time of the simulations, and not a permanent alteration in the nonlinear dynamics, unlike the PANS feedback mechanism. As such, the FSM variants show little improvement in error over SKE in the evolution of \mathcal{K}_m and $\mathcal{E}_m.$ However, all four FSM-like variants still demonstrate a reasonable agreement with the approximate dynamical system of Eq. (24), especially the simple global-coefficient FSM-Speziale and FSM- R_{vK} models.

The FSM-like models show considerably more variation in the expression of their underlying feedback mechanism as a function of κ_f

than does the PANS mechanism, as shown in Figs. 11 and 12. Here again, we show only the \mathcal{K}_m dynamics, and not the \mathcal{E}_m dynamics, for the sake of brevity. First, it can be seen that at $\kappa_f = 2,$ the dynamic-coefficient and f_{Δ} variants are initially identical to SKE RANS [Fig. 11, panels (b) and (e)], while the Speziale and R_{vK} -based models perturb the SKE dynamics from the initial conditions. FSM- f_{Δ} transitions to an LES-like C_{μ}^* mode around $t' = 4,$ while the dynamic coefficient model remains locked to the SKE model until very late times (i.e., $t' > 10$). Regardless, all four models show almost no feedback in $\mathcal{D}_{\mathcal{K}},$ which follows the SKE dynamics closely at all times [panel (f)].

In contrast, at $\kappa_f = 128,$ the $\langle \Pi_m \rangle / \mathcal{K}_r$ and $\mathcal{P}_{\mathcal{K}}$ terms of most variants experience very large initial perturbations compared to SKE [Fig. 12, panels (b) and (e)], with the exception being FSM- $f_{\Delta},$ which starts from the same smaller offsets as the k -SGS LES model for these terms. These perturbations, in turn, still lead to a permanent increase in $\mathcal{E}_r / \mathcal{K}_r$ [panel (c)] and initial decrease in $\mathcal{D}_{\mathcal{K}},$ followed by an asymptotic return of the production and destruction dynamics to the SKE RANS baseline [panels (e) and (f)]. However, the widely varying fractional reductions in $\langle \Pi_m \rangle$ are sufficient to enable each variant to achieve DNS-like behavior in the resolved turbulence dynamics [panel (a)]. If the only metric of whether an HRL model improved upon RANS was if it enhanced resolved turbulence fluctuations, it would appear that FSM-like models are successful. This result is often reported in tests of HRL models using complex wall-bounded flows at high Reynolds numbers, but is clearly an insufficient test of model performance.

C. DES-like models

Figure 13 shows the time evolution of the mean model dynamics of all five DES-like models, which includes CES-K and CES-X utilizing initial condition option #1 (IC1), at $\kappa_f = 2, 16,$ and $128.$ It can be seen that the three traditional DES-like variants (shades of purple) are

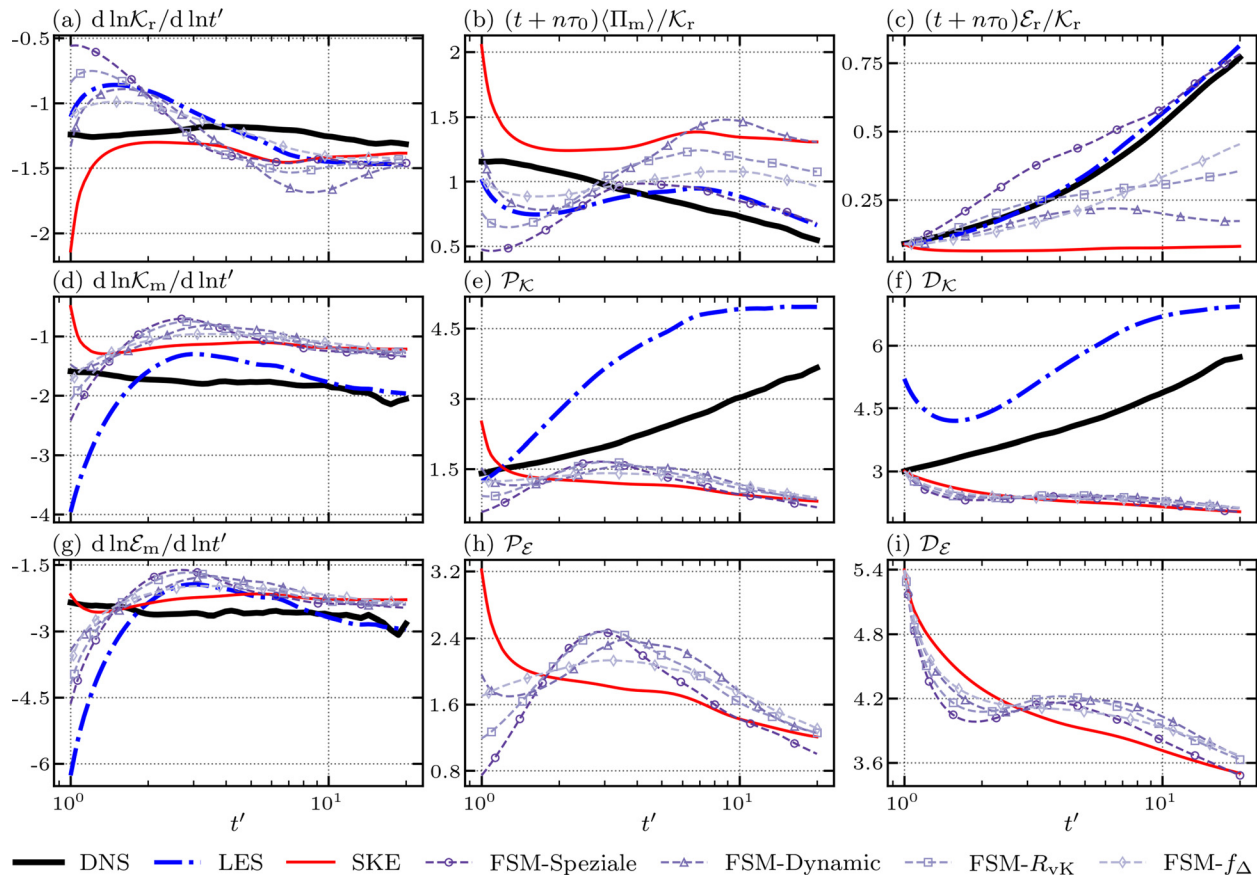


FIG. 10. Comparing the energy partitioning dynamics of the four FSM variants at filter wavenumber $\kappa_f = 16$. Shown are time series of (first row) (a) the instantaneous power-law exponent of K_r , (b) non-dimensional production rate of K_r , due to $\langle \Pi_m \rangle$, (c) non-dimensional production rate of K_r , due to \mathcal{E}_r ; (second row) (d) the instantaneous power-law exponent of K_m , (e) non-dimensional production rate of K_m , \mathcal{P}_K , (f) non-dimensional destruction rate of K_m , \mathcal{D}_K ; (third row) (g) the instantaneous power-law exponent of \mathcal{E}_m , (h) non-dimensional production rate of \mathcal{E}_m , \mathcal{P}_E , (i) non-dimensional destruction rate of \mathcal{E}_m , \mathcal{D}_E .

quantitatively very similar to each other at all three filter scales, as well as to the LES (blue) at the two finer scales, despite the fact that only XLES becomes mathematically equivalent to the k -SGS model when $C_{k2}^* > 1$. Conversely, these three variants are only similar to the two CES variants (shades of orange) at $\kappa_f = 2$, where the three traditional variants are mathematically equivalent to SKE (red) at $t' = 1$, and the two CES variants are very nearly equivalent ($C_{k2}^* \approx 1$). Despite this, the CES variants do behave qualitatively similar to LES and the other DES-like variants at $\kappa_f = 16$.

Overall, the traditional DES-like variants performs nearly identically to k -SGS LES for all $\kappa_f > 2$. The reason for this is made clear by inspection of the probability distributions of the length-scale ratio $C_{\Delta}\Delta/\ell_m$ for the standard DES model, shown in Fig. 14, which is representative of the behavior of all three variants and k -SGS. Distributions are plotted for every filter wavelength at three times, corresponding to the initial conditions, half a decay timescale later, and at the final conditions. For all resolutions $\kappa_f > 2$, the DES model initially behaves as a pointwise LES-RANS hybrid [Fig. 14(a)], with $C_{\Delta}\Delta/\ell_m < 0$ ($C_{k2}^* > 1$) at some points, while $C_{\Delta}\Delta/\ell_m > 0$ ($C_{k2}^* = 1$) at other points. However, the DES model rapidly suppresses these spatial fluctuations,

and, by $t' = 1.5$ [Fig. 14(b)], the PDFs of $C_{\Delta}\Delta/\ell_m$ collapse for resolutions $\kappa_f > 2$, indicating that it is operating as a two-equation LES model at nearly every point in the domain. For resolutions $\kappa_f \leq 2$, the DES starts in a purely SKE RANS mode at all points, but, at $\kappa_f = 2$, does make a slow transition to LES almost everywhere at later times [Fig. 14(c)].

This transition from RANS to LES at $\kappa_f = 2$ can be more clearly seen in Fig. 15, which shows time series of the dissipation-weighted average C_{k2}^* coefficient for DES, RG- τ , and CES-K. Both DES and RG- τ at $\kappa_f = 2$ begin the transition from RANS to hybrid RANS-LES starting at roughly $t' \approx 4$. In contrast, the simulation using CES-K, which utilizes a global coefficient to bridge between RANS and DNS, starts immediately as a hybrid model with $C_{k2}^* > 1$ at $t' = 1$ for $\kappa_f = 2$ and smoothly varies in time toward a similar final value of C_{k2}^* as in the simulations at $\kappa_f = 16$ and 128. Not shown are the $\{C_{k2}^*\}$ time series for XLES, which are very close to standard DES, and the C_{k2}^* time series for CES-X, which are essentially identical to CES-K.

To compare and contrast these models further, we must inspect their nonlinear power-law dynamics as defined by Eq. (23). Figure 16 shows the details of the nonlinear power-law dynamics of all five

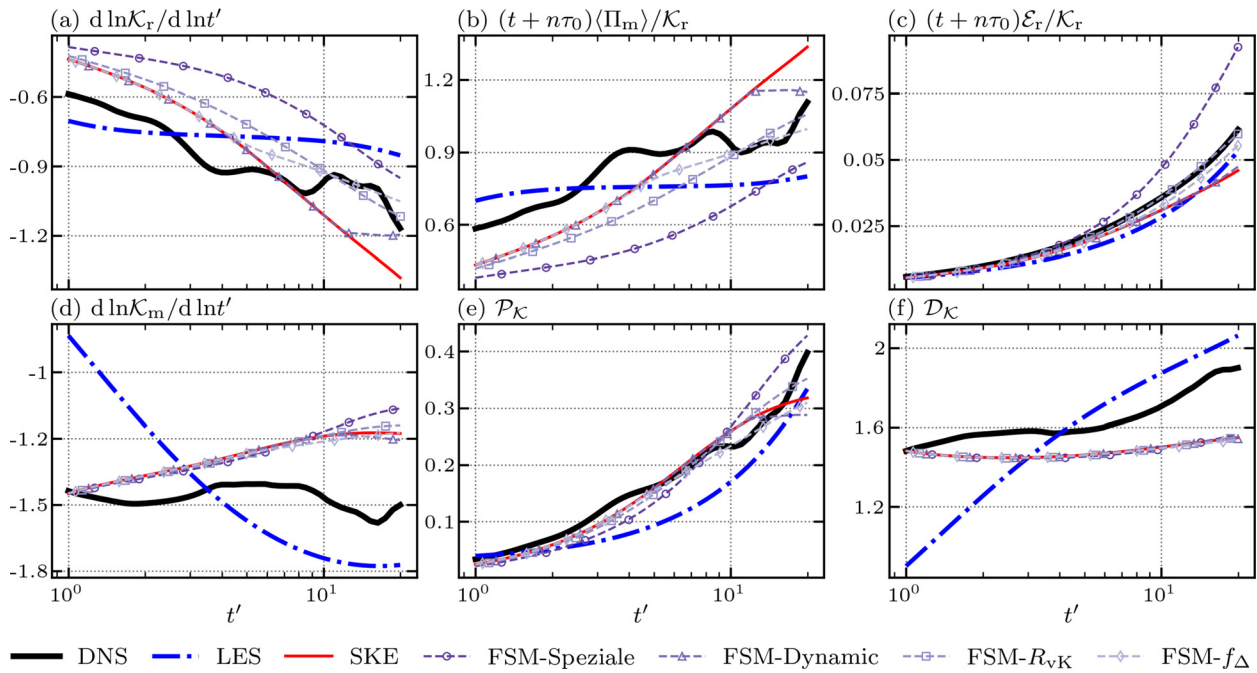


FIG. 11. Energy partitioning dynamics of the four FSM variants at the near-URANS limit of $\kappa_f = 2$. Shown are time series of (first row) (a) the instantaneous power-law exponent of \mathcal{K}_r , (b) non-dimensional destruction of \mathcal{K}_r due to $\langle \Pi_m \rangle$, (c) non-dimensional destruction of \mathcal{K}_r due to \mathcal{E}_r ; (second row) (d) the instantaneous power-law exponent of \mathcal{K}_m , (e) non-dimensional production rate of \mathcal{K}_m , $\mathcal{P}_{\mathcal{K}}$, (f) non-dimensional destruction rate of \mathcal{K}_m , $\mathcal{D}_{\mathcal{K}}$.

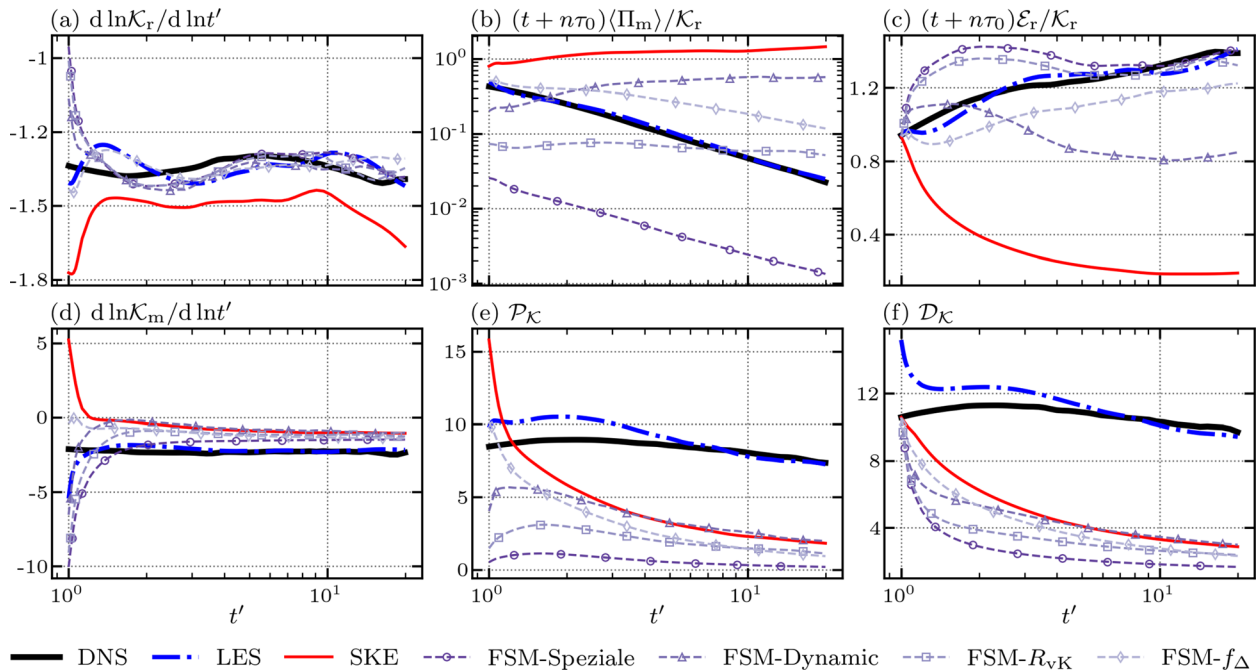


FIG. 12. Energy partitioning dynamics of the four FSM variants at the near-DNS limit of $\kappa_f = 128$. Shown are time series of (first row) (a) the instantaneous power-law exponent of \mathcal{K}_r , (b) non-dimensional destruction of \mathcal{K}_r due to $\langle \Pi_m \rangle$, (c) non-dimensional destruction of \mathcal{K}_r due to \mathcal{E}_r ; (second row) (d) the instantaneous power-law exponent of \mathcal{K}_m , (e) non-dimensional production rate of \mathcal{K}_m , $\mathcal{P}_{\mathcal{K}}$, (f) non-dimensional destruction rate of \mathcal{K}_m , $\mathcal{D}_{\mathcal{K}}$.

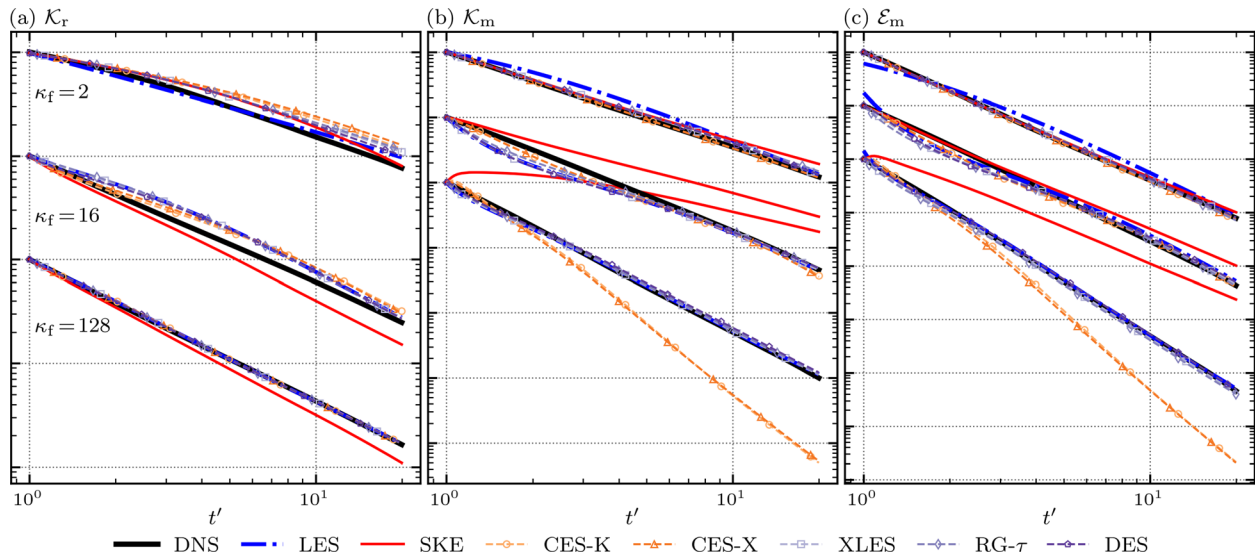


FIG. 13. Comparing the mean model dynamics of the five DES-like HRL variants at filter wavenumbers $\kappa_f = 2, 16,$ and 128 . Shown are time series of (a) mean resolved kinetic energy, \mathcal{K}_r , (b) mean modeled kinetic energy, \mathcal{K}_m , and (c) mean modeled dissipation, \mathcal{E}_m . Time series for all turbulence models are normalized by the corresponding filtered DNS value at $t = 0$ and then offset by a different fixed multiple for each κ_f and quantity of interest to show each subplot on a single vertical axis.

DES-like models at $\kappa_f = 16$. As with the PANS-like results, dynamics at this filter width are demonstrative of DES-like model behavior at all $\kappa_f > 2$. Once again, all five variants demonstrate a reasonable agreement with the approximate dynamical system of Eq. (24), with the global-coefficient CES variants having the highest degree of similarity, and RG- τ showing the weakest agreement.

Despite the large quantitative differences between the CES and traditional DES-like variants—as well as the more subtle differences between RG- τ and the closely aligned DES, XLES, and LES models—all five DES-like models prove to be qualitatively quite similar to each other, while behaving both quantitatively and qualitatively far different than SKE. The one commonality in all five HRL model forms is that they employ a C_{k2}^* coefficient and, by comparison to the FSM-like feedback, it is clear that the feedback mechanism driving all five models away from the baseline SKE dynamics must stem from this single shared aspect. Moreover, it is clear that the CES variants using the default IC1 initial condition behave essentially the same as they did when started with the PANS-like IC2 initial condition, except for the obvious difference in the starting values of their destruction terms. In contrast, the traditional DES-like models show some deviation from the PANS-like feedback mechanism at early times.

The reasons for these similarities and differences are made immediately obvious by inspection of Eq. (24). For global-valued coefficients, the perturbation made by an initial $C_{k2}^* > 1$ is to immediately make the temporal log-derivative of \mathcal{K}_m more negative (i.e., decay faster), thus decreasing \mathcal{K}_m relative to SKE, and making the ratio $\mathcal{E}_m/\mathcal{K}_m$ larger. While PANS-like models initially perturb \mathcal{E}_m in the opposite direction, the effect on the ratio $\mathcal{E}_m/\mathcal{K}_m$, as well as $\mathcal{K}_m^2/\mathcal{E}_m$, is the same, and thus both perturbations feedthrough the nonlinear system of equations by the same functional mechanism. That is, the destruction terms both instantly trend upward relative to SKE while the cross-filter transfer $\langle \Pi_m \rangle / \mathcal{K}_r$ instantly trends lower than SKE. These changes then lead to an increase in $\langle |\bar{S}|^2 \rangle$, followed by increases

in the production terms, and a permanent shift in the temporal derivatives away from SKE and toward DNS.

The principal difference between the global-coefficient CES models and the local-coefficient traditional DES-like variants comes at very early times ($t' < 2$), where $\mathcal{D}_\mathcal{K}$ shows a negative, rather than positive, initial slope. The reason for this is simply due to the rapid decrease in $\{C_{k2}^*\}$ from its initial value due to the suppression of the initial variance in the filtered-DNS distribution of f_Δ (see Figs. 14 and 15). Once this process is finished, the trend in $\mathcal{D}_\mathcal{K}$ for the traditional DES-like variants reverses and subsequently matches the behavior of the global-coefficient DES-like and PANS-like models.

While $C_{k2}^* > 1$ is the only initial perturbation made by the DES and CES-K variants, the XLES, RG- τ , and CES-X variants also modify C_{μ}^* and, therefore, perturb the initial values of $\langle \Pi_m \rangle$, $\mathcal{P}_\mathcal{K}$, and $\mathcal{P}_\mathcal{E}$ as well. Additionally, RG- τ perturbs both $\mathcal{P}_\mathcal{E}$ and $\mathcal{D}_\mathcal{E}$ via nonstandard C_{e1}^* and C_{e2}^* . In the cases of XLES and RG- τ , this results in $\langle \Pi_m \rangle$ starting at a much lower initial value than SKE rather than experiencing a rapid decrease away from the high SKE initial state. Similarly, $\mathcal{P}_\mathcal{K}$ and $\mathcal{P}_\mathcal{E}$ start low and only ever trend upward for k -SGS, XLES, and RG- τ . Finally, for the RG- τ model only, the initial rapid change in the distribution of f_Δ affects $\mathcal{D}_\mathcal{E}$ in the same manner as $\mathcal{D}_\mathcal{K}$.

Despite these initial differences, by $t' = 2$ DES, XLES and RG- τ are all roughly converged with the k -SGS LES net decay rates. Conversely, CES-K and CES-X are quantitatively close to each other for almost all time, due to the much smaller initial perturbations, but never converge with the LES trends. Add, the RG- τ model differs from DES and XLES by also perturbing the initial value of $\mathcal{D}_\mathcal{E}$. Therefore, none of the additional nonstandard coefficients beyond C_{k2}^* in these DES-like variants has a medium or long-term impact on the feedback mechanism induced by C_{k2}^* alone.

The nonlinear feedback mechanism of each DES-like model is qualitatively similar to that outlined above for all κ_f and t' where $C_{k2}^* > 1$, though there are quantitative differences. Most notably, for

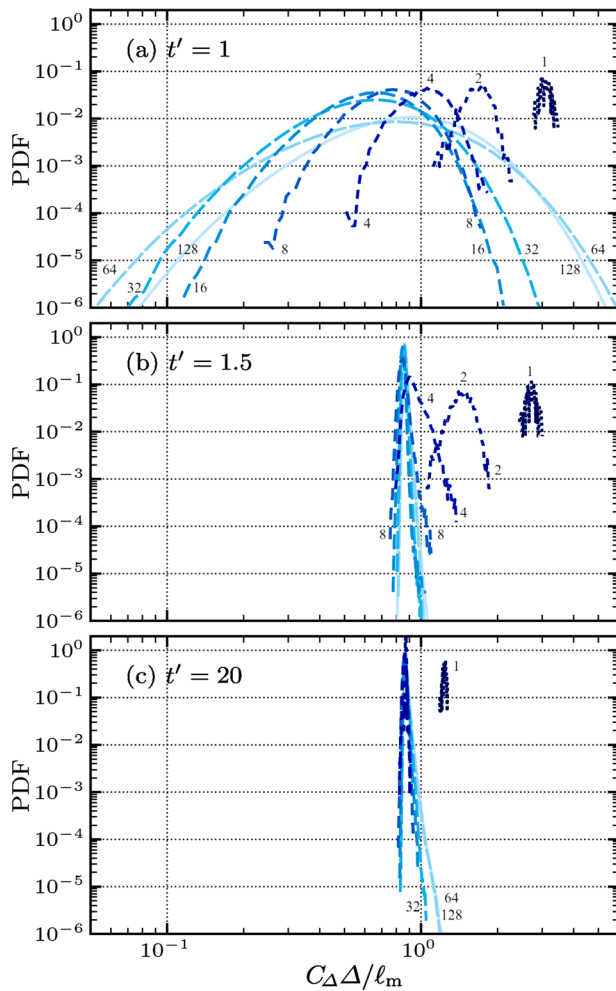


FIG. 14. Probability density functions of $C_{\Delta} \Delta / \ell_m$, for standard DES with $C_{\Delta} = 0.61$, at (a) the initial condition, $t' = 1$, (b) one-half decay time later, $t' = 1.5$, and (c) $t' = 20$, and for each filter wavenumber $1 \leq \kappa_f \leq 128$. Line styles and colors are the same as in Fig. 3.

$\kappa_f = 2$, DES, XLES, and RG- τ are all initially identical to the baseline SKE, with $C_{k2}^* = 1$ at all points, and these dynamics are shown in Fig. 17. Because of the strong dynamical similarity between production and destruction terms demonstrated previously, we show only the \mathcal{K}_m dynamics, and not those of \mathcal{E}_m .

The nonlinear feedback mechanism for standard DES starts as a positive perturbation in the trend of $\mathcal{D}_{\mathcal{K}}$ after $t' = 4$ [panel (f)], rather than as an instantaneous offset at $t' = 1$. However, increasing values of $\mathcal{D}_{\mathcal{K}}$ kick off the same feedback sequence for standard DES, starting with a less positive trend in $\langle \Pi_m \rangle / \mathcal{K}_r$ [panel (b)] and a more positive trend in $\mathcal{D}_{\mathcal{E}}$ (not shown) about $t' = 5$. This in turn induces more positive trends in $\mathcal{E}_r / \mathcal{K}_r$ [panel (c)], $\mathcal{P}_{\mathcal{K}}$ [panel (e)], and $\mathcal{P}_{\mathcal{E}}$ (not shown) just before $t' = 10$.

As before, XLES and RG- τ differ from standard DES by also inducing negative changes at $t' = 4$ in $\langle \Pi_m \rangle / \mathcal{K}_r$, $\mathcal{P}_{\mathcal{K}}$, and $\mathcal{P}_{\mathcal{E}}$ with respect to SKE, due to the decreasing value of C_{μ}^* as f_{Δ} drops below

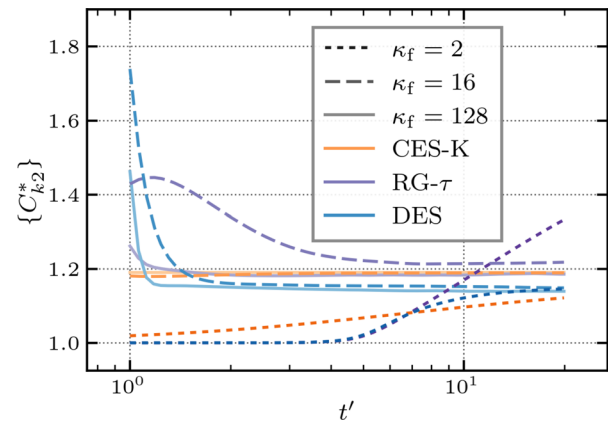


FIG. 15. Time series of the dissipation-weighted average C_{k2}^* coefficient, $\{C_{k2}^*\} = \langle C_{k2}^* \mathcal{E}_m \rangle / \langle \mathcal{E}_m \rangle$, for DES, RG- τ , and CES-K, at $\kappa_f = 2, 16$, and 128 .

unity, though the initial perturbation in the production terms is much more subtle than for $\langle \Pi_m \rangle / \mathcal{K}_r$. From there a more positive trend is induced in $\mathcal{E}_r / \mathcal{K}_r$ (and therefore $\langle |\bar{S}|^2 \rangle$), which allows $\mathcal{P}_{\mathcal{K}}$ and $\mathcal{P}_{\mathcal{E}}$ to continue to increase, even as SKE stops increasing at late times. In contrast, CES-K and CES-X are not exactly equivalent to the baseline SKE at $t' = 1$ and increasingly diverge from SKE from the beginning of the simulations. Therefore, the CES variants generally follow all of the same trends as in Fig. 16 at $\kappa_f = 16$.

To demonstrate that these same nonlinear feedback mechanisms continues through to DNS, we also show the dynamics of the DES-like models at $\kappa_f = 128$ in Fig. 18, which differ from those shown in Fig. 16 in two ways: (i) due to the near-DNS resolution of the resolved turbulence dynamics, there is substantially reduced error in \mathcal{K}_r and \mathcal{E}_r [panels (a) and (c)], and (ii) the nonlinear feedback progresses through the dynamics much faster than for $\kappa_f = 16$, such that there is a much shorter intermediate time range, and a protracted late-time behavior. In the case of DES, XLES, and RG- τ , the late-time behavior matches that of the filtered DNS truth nearly exactly, while CES-K and CES-X both overshoot the DNS decay rates, resulting in excess destruction of \mathcal{K}_m and \mathcal{E}_m . The qualitative differences between $\kappa_f = 16$ and $\kappa_f = 128$ for all five models represent a consistent trend as κ_f is varied from 4 to 128.

V. SUMMARY AND CONCLUSIONS

Hybrid RANS-LES models that can accurately reproduce unsteady 3D flow physics across the entire range of grid scales and turbulence dynamics between URANS and DNS, but especially at resolutions coarser than typical LES, are important subjects of continued research and development. Recent examinations of HRL modeling concepts have outlined potential drawbacks to using traditional models like DES and FSM that are not shared by more modern variable-resolution bridging models, such as the PANS, PITM, and CES models, which seek to analytically derive a resolution-sensitive RANS model form that can span between URANS and DNS without transitioning through a distinct LES mode of operation. Unfortunately, these deficiencies are routinely under-emphasized due to a persistent and widespread focus on testing model performance in wall-bounded industrial and aerospace flows. This has limited the development of formal V&V procedures for HRL models, and, to our knowledge, no

systematic or comprehensive comparisons between a wide range of HRL model forms have ever been published.

In the present study, we chose to evaluate thirteen distinct HRL models via systematic grid refinement of decaying HIT using a single minimal-error numerical implementation. We formulated each of the thirteen models as unique realizations of a generalized form of the standard k - ϵ (SKE) RANS model, namely Eqs. (10a) and (10b). Thus, each HRL model is a direct modification of the SKE model, and we can think of the SKE model as a mathematical baseline that each model attempts to improve upon. Each model was also classified as DES-like, PANS-like, or FSM-like, depending on which coefficients of Eqs. (10a) and (10b) were modified from the SKE baseline. Among the DES-like models, DES itself, XLES, and RG- τ all behave more or less like one-equation differential LES models at fine resolutions. Therefore, all thirteen HRL models were evaluated against the one-equation k -SGS LES model in addition to the SKE model, as a performance baseline that each HRL should improve upon.

Because of the approximate power-law decay in all dynamical and kinematic quantities of interest over time, and the rapid accumulation of potentially large errors compared to the filtered DNS ground truth, we assessed the energy partitioning dynamics of each HRL model by performing an analysis of the non-dimensional logarithmic-time governing equations of \mathcal{K}_r , \mathcal{K}_m , and \mathcal{E}_m that represent the evolution of the instantaneous power-law decay exponents of each quantity. Moreover, we can interpret model-to-model variations in the energy partitioning, as dictated by the three decay exponents, as different nonlinear feedback mechanisms operating on a low-dimensional dynamical system. This analysis is similar to the dynamical system fixed-point analysis utilized in some previous works assessing URANS and bridging HRL models. The primary difference here is that we do not approximate the full high-dimensional dynamics with a closed set of ODEs that form a solvable low-dimensional system. Instead, we directly solve the high-dimensional system (i.e., perform 3D simulations) and then rely on an unclosed set of ODEs that approximate a low-dimensional dynamical system to simplify our interpretation and understanding of the high-dimensional results.

We found that every kind of HRL model, compared to the SKE baseline, can achieve a very accurate evolution of \mathcal{K}_r as resolution increases toward DNS. Despite this, the FSM-like models were shown to have dynamically inconsistent evolutions of \mathcal{K}_m and \mathcal{E}_m for all scale-resolving filter sizes. In contrast, the traditional DES-like models (DES, XLES, and RG- τ) show a high degree of accuracy in all metrics at $\kappa_f \geq 16$, where they all perform essentially identically to k -SGS LES, despite having unique theoretical derivations and significant mathematical differences in their underlying LES model forms. As predicted by Chaouat,¹¹ the PANS-like models perform the best at very coarse resolutions $1 < \kappa_f < 16$, with the CES variants (operating as PANS-like models, based on initial conditions) being especially accurate. However, the CES variants become increasingly inaccurate relative to PANS and PITM as the filter resolution approaches DNS. CES was formulated assuming very high Re or coarse grids where $F_e \approx 1$. This is typical of aerospace flows, but not necessarily all engineering turbulence flows of interest (such as inertial confinement fusion); therefore, it is not surprising that CES behaves poorly at fine resolutions where $F_e < 1$.

A particularly interesting result is that the initial increase in $\mathcal{D}_{\mathcal{K}}$ by DES-like models and decrease in $\mathcal{D}_{\mathcal{E}}$ by PANS-like models are dynamically similar interventions, as they both act to increase $\mathcal{E}_m/\mathcal{K}_m$,

which stimulates the same subsequent nonlinear feedback mechanism. This *qualitative* dynamical equivalence is inherent to the model forms and does not require constructing *quantitatively* equivalent models via variational analysis to demonstrate a connection between DES and PANS. Indeed, we showed that the DES-like, CES-K, and CES-X models can be induced to give nearly identical results to the PANS-like CES-S model simply by changing the initial values of ϵ_m by a constant multiple. A graphical depiction of the nonlinear feedback mechanisms, which result from our analysis for standard DES (which is the dominant mechanism for all three of the traditional DES-like models), PANS-like models, and FSM-like models is shown in Fig. 19 for a visual side-by-side comparison of the qualitative similarities and differences in how each model type functions.

Since in this study, we used carefully-implemented decaying HIT that follows a power-law trend, we know that URANS is highly accurate at capturing the spatially-averaged trends, and we know that k -SGS LES will be highly accurate so long as the peak in the energy spectrum is resolved. This should not be a challenging test for any model. Instead, decaying HIT with a power law trend is a test that a robust model should be expected to pass. In general, these results indicate that variable-resolution bridging based on the $C_{\epsilon_2}^*$ coefficient provide the best HRL capability for two-equation models at the coarse resolutions that are practical for real-world flows of interest. However, this HRL model form can only become “universal” or “one-model-fits-all-cases” (that is, competitive with quality LES models at fine resolutions) with additional development work.

Extending the analysis to flows with one or more directions of inhomogeneity may result in changes to some feedback mechanisms, as additional terms would appear in the governing equations of the decay rates Eqs. (25a)–(25c). Testing models in the context of a well-characterized canonical flow case with just one direction of inhomogeneity, such as 3D Rayleigh–Taylor instability or temporal shear driven mixing layer, would be a logical next step in a complete V&V process.

ACKNOWLEDGMENTS

C.A.Z.T. is grateful to Dr. Fernando Grinstein and Dr. Daniel Israel for insightful conversations regarding HRL modeling and V&V. This work has been authored by employees of Triad National Security, LLC which operates Los Alamos National Laboratory (LANL) under Contract No. 89233218CNA000001 with the U.S. Department of Energy/National Nuclear Security Administration. We acknowledge support from LANL’s Laboratory Directed Research and development (LDRD) program, Project Nos. 20190059DR and 20220104DR, from LANL’s Advanced Simulation and Computing (ASC) Physics and Engineering (PEM) Mix&Burn project, and from LANL’s Office of Experimental Sciences (OES), and computational resources from LANL’s Institutional Computing (IC) program.

AUTHOR DECLARATIONS

Conflict of Interest

The authors have no conflicts to disclose.

Author Contributions

Colin A. Z. Towery: Conceptualization (equal); Data curation (lead); Formal analysis (equal); Investigation (equal); Methodology (equal);

Software (lead); Validation (lead); Visualization (lead); Writing – original draft (lead); Writing – review & editing (equal). **Juan A. Saenz:** Conceptualization (equal); Formal analysis (equal); Funding acquisition (supporting); Investigation (equal); Methodology (equal); Project administration (supporting); Resources (equal); Supervision (equal); Writing – original draft (supporting); Writing – review & editing (equal). **Daniel Livescu:** Conceptualization (equal); Formal analysis (equal); Funding acquisition (lead); Investigation (equal); Methodology (equal); Project administration (lead); Resources (equal); Supervision (equal); Writing – original draft (supporting); Writing – review & editing (equal).

DATA AVAILABILITY

The data that support the findings of this study are available from the corresponding author upon reasonable request.

APPENDIX A: ACCURACY OF THE CES-U VARIANT

We showed in Figs. 16–18 that the standard DES and XLES models had extremely similar dynamics and accuracy over all times

$t' > 2$, and that their CES counterparts, CES-K and CES-X, are equally consistent with each other, indicating the essential importance of the C_{k2}^* coefficient compared to C_{μ}^* . However, in Heinz,³⁶ the CES-KEKU variation meant to correspond to XLES (also known as Uni-LES), and which we refer to as CES-U, has a formula for C_{k2}^* that differs from CES-K and CES-X by a power of two,

$$\text{CES-K/X: } C_{k2}^* = \gamma - R_{ces}(\gamma - 1),$$

$$\text{CES-U: } C_{k2}^* = [\gamma - R_{ces}(\gamma - 1)]^{1/2}.$$

This is a critical difference that, while having the same qualitative nonlinear feedback mechanism, leads to a large quantitative difference in accuracy, as demonstrated in Fig. 20. As such, we chose to present only the results of CES-X, and not CES-U, in Sec. IV.

APPENDIX B: FURTHER DETAILS OF THE NUMERICAL METHODS AND HRL MODEL STABILITY

The pseudo-spectral CFD was developed in a highly modular fashion using object-oriented programming principles, starting with the DNS functionality of the shenfun⁴⁵ Python package

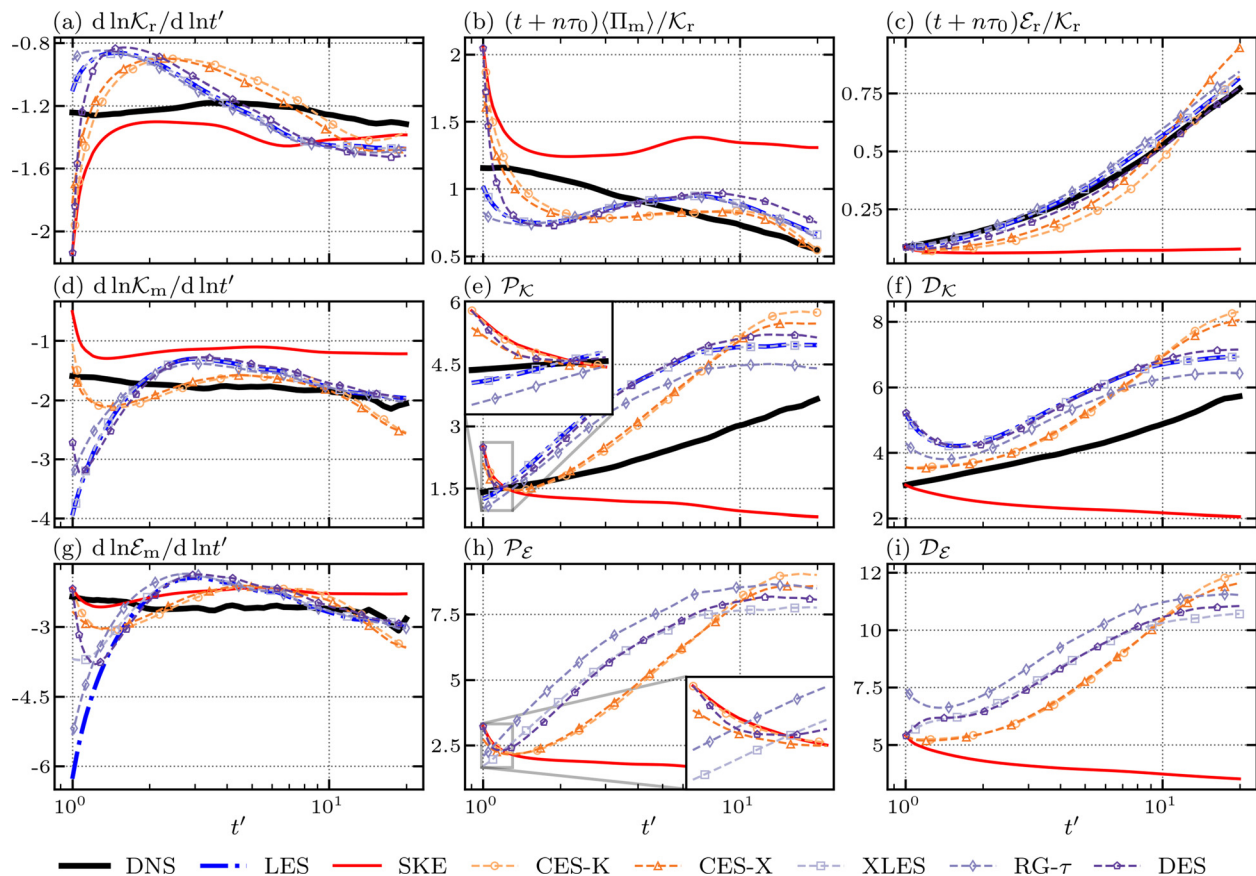


FIG. 16. Comparing the energy partitioning dynamics of the five DES-like HRL variants at filter wavenumber $\kappa_f = 16$. Shown are time series of (first row) (a) the instantaneous power-law exponent of K_r , (b) non-dimensional destruction of K_r due to $\langle \Pi_m \rangle$, (c) non-dimensional destruction of K_r due to E_r ; (second row) (d) the instantaneous power-law exponent of K_m , (e) non-dimensional production rate of K_m , P_K , (f) non-dimensional destruction rate of K_m , D_K ; (third row) (g) the instantaneous power-law exponent of E_m , (h) non-dimensional production rate of E_m , P_E , (i) non-dimensional destruction rate of E_m , D_E .

07 October 2024 15:15:00

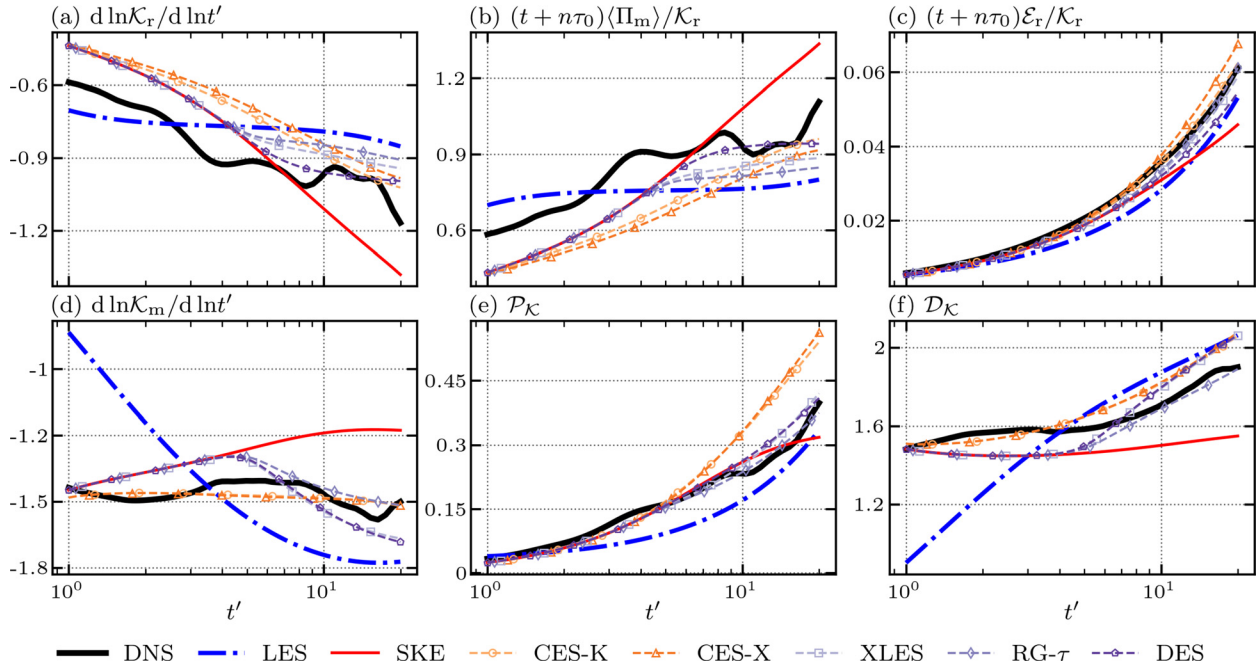


FIG. 17. Energy partitioning dynamics of the five DES-like HRL variants at the near-URANS limit of $\kappa_{fi} = 2$. Shown are time series of (first row) (a) the instantaneous power-law exponent of \mathcal{K}_r , (b) non-dimensional destruction of \mathcal{K}_r due to $\langle \Pi_m \rangle$, (c) non-dimensional destruction of \mathcal{K}_r due to \mathcal{E}_r ; (second row) (d) the instantaneous power-law exponent of \mathcal{K}_m , (e) non-dimensional production rate of \mathcal{K}_m , $\mathcal{P}_{\mathcal{K}}$, and (f) non-dimensional destruction rate of \mathcal{K}_m , $\mathcal{D}_{\mathcal{K}}$.

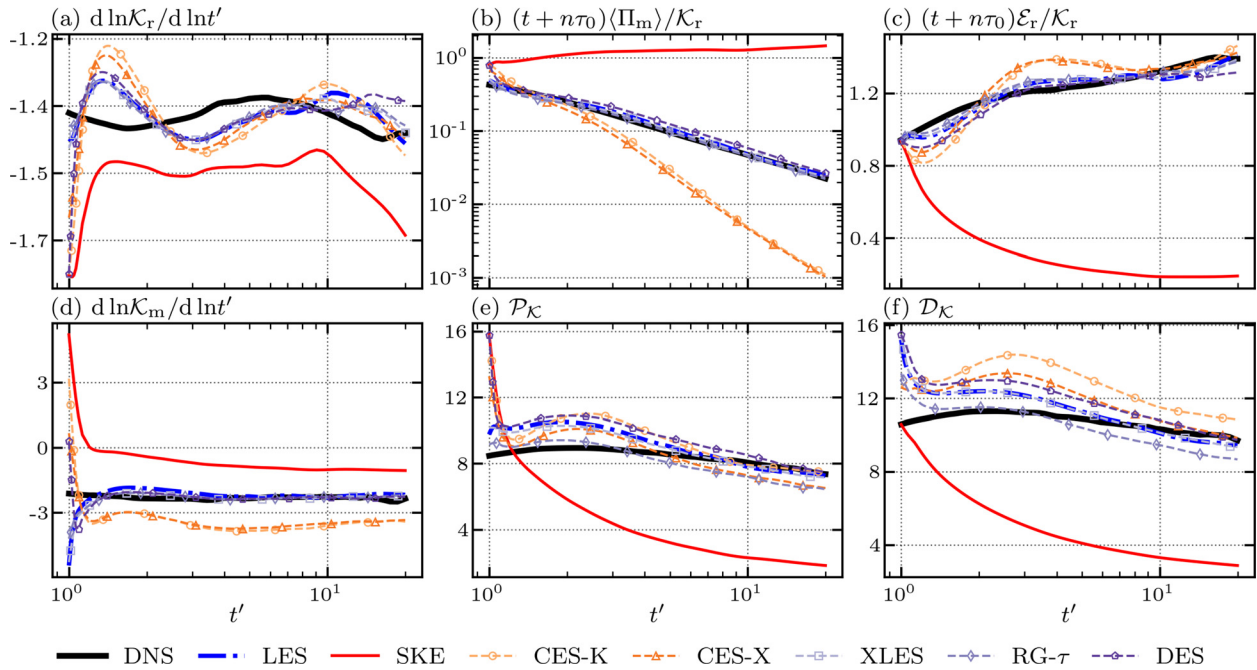


FIG. 18. Energy partitioning dynamics of the five DES-like HRL variants at the near-DNS limit of $\kappa_{fi} = 128$. Shown are time series of (first row) (a) the instantaneous power-law exponent of \mathcal{K}_r , (b) non-dimensional destruction of \mathcal{K}_r due to $\langle \Pi_m \rangle$, (c) non-dimensional destruction of \mathcal{K}_r due to \mathcal{E}_r ; (second row) (d) the instantaneous power-law exponent of \mathcal{K}_m , (e) non-dimensional production rate of \mathcal{K}_m , $\mathcal{P}_{\mathcal{K}}$, and (f) non-dimensional destruction rate of \mathcal{K}_m , $\mathcal{D}_{\mathcal{K}}$.

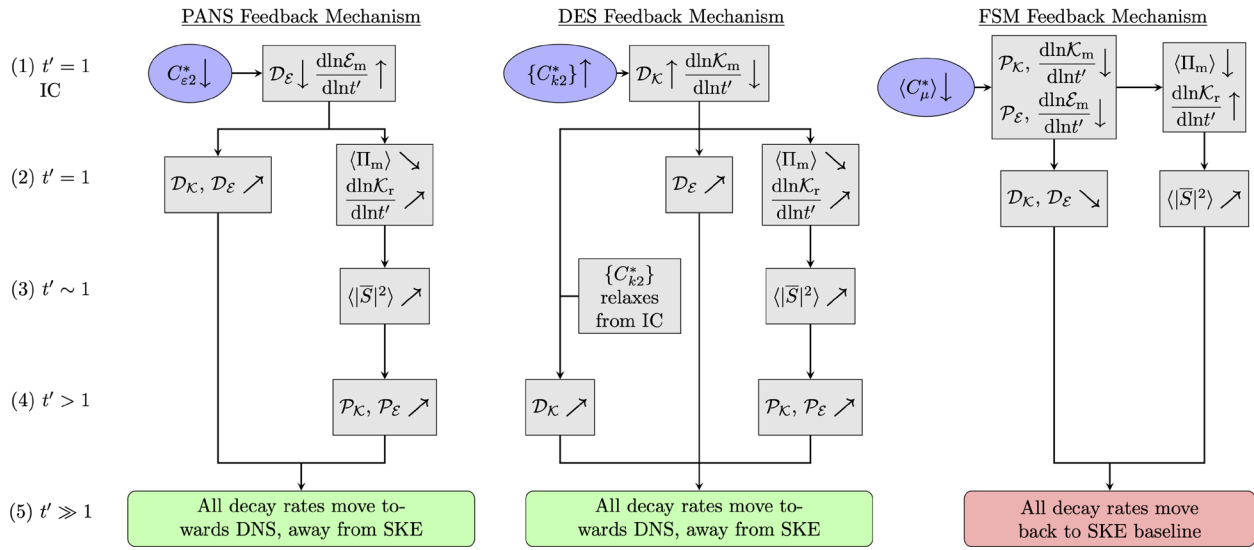


FIG. 19. Summary flowcharts of the standard DES (left), PANS-like (center), and FSM-like (right) nonlinear feedback mechanisms, showing (1) the initial perturbation at $t' = 1$, (2) primary (instantaneous) feedback at $t' = 1$, (3) secondary (fast) changes at very early times, $t' \sim 1$, (4) tertiary (slow) changes at intermediate times, $t' > 1$, and (5) the end result at very late times, $t' \gg 1$. Arrows indicate changes relative to SKE model baseline.

demonstrated using a simple Taylor–Green Vortex (TGV) simulator in the `spectralDNS` code repository.⁵² Throughout the code development, any changes made to the core Navier–Stokes solver class were verified using the TGV test case, as in the original demonstration code. From there, unit-tested functions for spectral-space

smooth filtering, mesh resizing, bandpass linear turbulence forcing, and runtime data co-processing, including parallelized statistical operations such as multi-dimensional histograms, were implemented. These capabilities were collectively validated by DNS of decaying and forced HIT against our previous DNS codes.⁴⁸

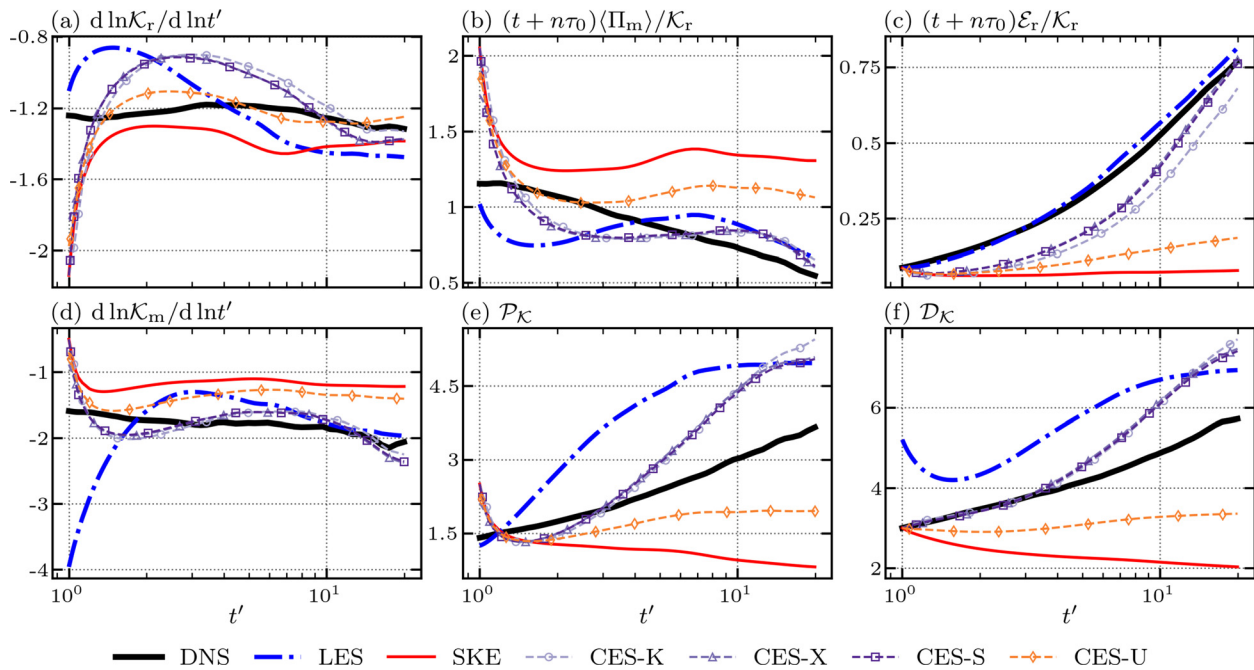


FIG. 20. Comparing the nonlinear dynamics of CES-U to the other CES variants given in Sec. II C at $\kappa_f = 16$. Here CES variants K, X, and U all use initial condition IC2 for direct comparison to CES-S. All sub-captions and the lines for filtered DNS, LES, and SKE are the same as in Fig. 16.

The DNS solver base class was then extended sequentially to algebraic LES, one-equation LES, and two-equation RANS capabilities. The static Smagorinsky model,²⁵ which has very well-described behavior for forced HIT, was used as the initial algebraic LES validation case, and then the dynamic Smagorinsky model using the Germano-Lilly procedure⁴⁰ was tested, providing verification of the mathematical functions required for dynamic coefficient computations. From there the baseline k -SGS one-equation LES model was added, the correctness of the numerical k transport equation was verified, and LES solutions were validated against the Smagorinsky results. Next, the standard k - ε two-equation RANS model was added, the correctness of 3D URANS of decaying HIT was verified on several different mesh sizes and then resolved SKE simulations were validated against the k -SGS LES results. Finally, generalized k - ε HRL capability was added by replacing the SKE RANS constants with 3D variables updated via external function calls, which were individually verified as each HRL model was implemented. Validation testing of the decaying HIT case using SKE, XLES, and PANS coefficient functions revealed sufficient numerical instability to warrant implementation and testing of higher-order dealiasing procedures as well as Gaussian filtering of the full right-hand side calculations. When these procedures proved to be unacceptable in either computational cost or fidelity, the HRL class was re-implemented using positivity-preserving $\ln k$ - $\ln \varepsilon$ transport equations.

From Ilinca and Pelletier,⁵¹ a change in model solution variables to $v_1 = \ln k_m$ and $v_2 = \ln \varepsilon_m$ gives

$$\frac{\partial v_1}{\partial t} + \bar{u}_j \frac{\partial v_1}{\partial x_j} = \frac{\partial}{\partial x_j} \left[\left(\nu + \frac{\nu_m}{\sigma_k} \right) \frac{\partial v_1}{\partial x_j} \right] + \left(\nu + \frac{\nu_m}{\sigma_k} \right) \frac{\partial v_1}{\partial x_j} \frac{\partial v_1}{\partial x_j} + e^{-v_1} (\Pi_m - C_{k2}^* e^{v_2}), \tag{B1a}$$

$$\frac{\partial v_2}{\partial t} + \bar{u}_j \frac{\partial v_2}{\partial x_j} = \frac{\partial}{\partial x_j} \left[\left(\nu + \frac{\nu_m}{\sigma_\varepsilon} \right) \frac{\partial v_2}{\partial x_j} \right] + \left(\nu + \frac{\nu_m}{\sigma_\varepsilon} \right) \frac{\partial v_2}{\partial x_j} \frac{\partial v_2}{\partial x_j} + e^{-v_1} (C_{\varepsilon 1}^* \Pi_m - C_{\varepsilon 2}^* e^{v_2}), \tag{B1b}$$

$$\nu_m = C_\mu^* \exp(v_1^2 - v_2),$$

which are identical except for the σ and C^* coefficients and include one additional non-conservative term compared to Eqs. (10a) and (10b). This change in the solution variable ensures that k_m and ε_m remain positive at all times by construction. When using the pseudo-spectral discretization method with 2/3 rds dealiasing, only the left hand-side advection terms of Eqs. (B1a) and (B1b), which have quadratic nonlinearity, are fully dealiased. All right-hand side (RHS) terms have higher nonlinearities and, therefore, are incompletely dealiased. Nevertheless, the production and destruction terms, $e^{-v_1} \Pi_m$ and $e^{v_2 - v_1}$, should be strictly positive quantities. However, using spectrally sharp dealiasing, the physical-space reconstruction of these terms, post-dealiasing, can include negative values. Although these non-positive values are never directly computed when integrating the solution forward in time, this non-realizability is implicit in the numerical method. It is this combination of RHS aliasing and non-positivity that gives rise to numerical instabilities in performing HRL simulations. As such, after initial verification tests of each model, we comprehensively tested a few representative models (SKE, XLES, and PITM) at $\kappa_f \in [2, 8, 32, 128]$ with various grid resolutions, $\Delta/\delta x \in [1, 2, 3, 4]$, with and without

initial condition (IC) smoothing, and with and without RHS smoothing. The IC smoothing procedure reapplies the same Gaussian filter as used to compute \bar{u}_i to the initial values of k_m and ε_m . This does not affect the mean values \mathcal{K}_m and \mathcal{E}_m but reduces their variances before converting the fields to v_1 and v_2 . The RHS smoothing procedure applies the same Gaussian filter to the computed ν_m and then filters the sum of the non-conservative RHS terms prior to dealiasing.

For nearly all κ_f , we found that using a high resolution mesh ($\Delta/\delta x = 3$) was sufficient to provide an accurate and stable solution. At $\kappa_f = 128$, $\Delta/\delta x = 3$ corresponds to a 768^3 physical-space mesh, and we found solving the HRL equations on this mesh size to be prohibitively expensive when comparing so many models. As such we limited the simulations to $\Delta/\delta x = 2$ at $\kappa_f = 128$ to reduce computational cost. For SKE and PITM, there was no significant decrease in accuracy. However, for XLES, there was an increased, though not substantial, impact on numerical stability and accuracy at early times, before turbulence viscosity smoothed out most of the spatial variance in the filtered DNS initial conditions (see Fig. 14). Therefore, we activated IC smoothing for all HRL models at $\kappa_f = 128$. In contrast, we found that RHS smoothing did not significantly improve accuracy of the solutions once IC smoothing was activated, but did have an additional impact by allowing for larger dynamic time step sizes, and therefore, provided additional savings in overall computational cost of the large-scale simulations.

APPENDIX C: RESPONSE OF THE DES-LIKE MODELS TO A PANS-LIKE MODIFICATION OF THE INITIAL CONDITIONS

The CES-K and CES-X models, having global non-unity C_{k2}^* values, can utilize two different initial conditions, based upon the DNS-derived dissipation, to slightly alter behavior. Denoting the correct initial subgrid-scale dissipation rate as ε_{sgs}^0 , the first initial condition (IC1) initializes $\varepsilon_m^0 = \varepsilon_{sgs}^0$, leading the initial modeled dissipation of k_m in Eq. (10a) to be greater than the correct rate, $C_{k2}^* \varepsilon_m^0 > \varepsilon_{sgs}^0$. The second initial condition (IC2) initializes $\varepsilon_m^0 = \varepsilon_{sgs}^0 / C_{k2}^*$ such that $C_{k2}^* \varepsilon_m^0 \equiv \varepsilon_{sgs}^0$. It was shown in Sec. IV that IC1 allows CES-K and CES-X to behave as DES-like while IC2 allows these models to behave as PANS-like, without any modification to the model forms themselves.

The traditional DES-like models, which have localized C_{k2}^* values, cannot utilize IC2 to alter their nonlinear feedback behavior. When started with IC2, standard DES, XLES, and RG- τ simulations revert almost exactly to the temporal trajectories of their corresponding IC1 simulations within two time steps. The reason for this behavior is due to the use of a local rather than global C_{k2}^* and can be demonstrated *a priori* by a simple approximation as follows. First, recall for the standard DES model that $C_{k2}^* = f_\Delta^{-1}$ and so wherever $f_\Delta < 1$, $C_{k2}^* = \ell_m / (C_\Delta \Delta)$. Now, if we consider a DES that is initialized via IC2 and assume that the first time step is vanishingly small ($\delta t \approx 0$), the initialization and first time step of a simulation proceeds as follows:

1. Set $\ell_m^0 = \frac{(k_m^0)^{3/2}}{\varepsilon_{sgs}^0}$ for computation of f_Δ^0 .
2. Where $f_\Delta^0 < 1$, set $\varepsilon_m^0 = f_\Delta^0 \varepsilon_{sgs}^0 = C_\Delta \Delta \frac{(\varepsilon_{sgs}^0)^2}{(k_m^0)^{3/2}}$

3. Assume $\delta t \approx 0$ such that $k_m^1 = k_m^0$ and $\varepsilon_m^1 = \varepsilon_m^0$.
4. Now set $\ell_m^1 = \frac{(k_m^1)^{3/2}}{\varepsilon_m^1} = \frac{(k_m^0)^{3/2}}{C_A \Delta (\varepsilon_m^0)^{2/3}}$
5. This leads to the condition that $f_\Delta^1 = (f_\Delta^0)^2$, and the destruction of k_m^1 becomes $\varepsilon_{sgs}^1 = \frac{\varepsilon_m^1}{f_\Delta^1} = \frac{\varepsilon_{sgs}^0}{f_\Delta^0}$ which is the IC1 initial state.

Thus, for an infinitesimally-small time step, the IC2 ε_m and C_{k2}^* values transform exactly into those of IC1. In practice, our choice of an initial very small time step that is limited from growing more than two times larger from step-to-step follows this approximation very closely, if not exactly.

REFERENCES

- 1P. Spalart, W.-H. Jou, M. Strelets, and S. Allmaras, *Advances in DNS/LES*, edited by C. Liu and Z. Liu (Greyden Press, 1997).
- 2J. N. Sørensen, "Aerodynamic aspects of wind energy conversion," *Annu. Rev. Fluid Mech.* **43**, 427 (2011).
- 3Y. Zhou, "Rayleigh–Taylor and Richtmyer–Meshkov instability induced flow, turbulence, and mixing. I," *Phys. Rep.* **720–722**, 1–136 (2017).
- 4Y. Zhou, "Rayleigh–Taylor and Richtmyer–Meshkov instability induced flow, turbulence, and mixing. II," *Phys. Rep.* **723–725**, 1–160 (2017).
- 5D. Livescu, "Turbulence with large thermal and compositional density variations," *Annu. Rev. Fluid Mech.* **52**, 309 (2020).
- 6P. A. Bogenschutz, A. Gettelman, H. Morrison, V. E. Larson, C. Craig, and D. P. Schanen, "Higher-order turbulence closure and its impact on climate simulations in the community atmosphere model," *J. Clim.* **26**, 9655–9676 (2013).
- 7A. G. Nouri, P. Givi, and D. Livescu, "Modeling and simulation of turbulent nuclear flames in Type Ia supernovae," *Prog. Aerosp. Sci.* **108**, 156 (2019).
- 8D. M. Israel, "The myth of URANS," *J. Turbul.* **24**(8), 367–392, 2023.
- 9J. Fröhlich and D. Von Terzi, "Hybrid LES/RANS methods for the simulation of turbulent flows," *Prog. Aerosp. Sci.* **44**, 349 (2008).
- 10P. Sagaut, M. Terracol, and S. Deck, *Multiscale and Multiresolution Approaches in Turbulence—LES, DES and Hybrid RANS/LES Methods: Applications and Guidelines* (World Scientific, 2013).
- 11B. Chaouat, "The state of the art of Hybrid RANS/LES modeling for the simulation of turbulent flows," *Flow, Turbul. Combust.* **99**, 279 (2017).
- 12S. Heinz, "A review of hybrid RANS-LES methods for turbulent flows: Concepts and applications," *Prog. Aerosp. Sci.* **114**, 100597 (2020).
- 13F. S. Pereira, L. Eça, G. Vaz, and S. S. Girimaji, "Toward predictive RANS and SRS computations of turbulent external flows of practical interest," *Arch. Comput. Methods Eng.* **28**, 3953 (2021).
- 14F. S. Pereira, F. F. Grinstein, D. M. Israel, and L. Eça, "Verification and validation: The path to predictive scale-resolving simulations of turbulence," *J. Verif. Validation Uncertainty Quantif.* **7**, 021003 (2022).
- 15P. R. Spalart, "Detached-eddy simulation," *Annu. Rev. Fluid Mech.* **41**, 181 (2009).
- 16S. S. Girimaji and K. Abdol-Hamid, "Partially-averaged Navier Stokes model for turbulence: Implementation and validation," AIAA Paper No. AIAA 2005-502, 2005.
- 17S. S. Girimaji, "Partially-averaged Navier-Stokes model for turbulence: A Reynolds-averaged Navier-Stokes to direct numerical simulation bridging method," *J. Appl. Mech.* **73**, 413 (2006).
- 18B. Chaouat and R. Schiestel, "A new partially integrated transport model for subgrid-scale stresses and dissipation rate for turbulent developing flows," *Phys. Fluids* **17**, 065106 (2005).
- 19B. Chaouat and R. Schiestel, "Progress in subgrid-scale transport modelling for continuous hybrid non-zonal RANS/LES simulations," *Int. J. Heat Fluid Flow* **30**, 602 (2009).
- 20C. G. Speziale, "Turbulence modeling for time-dependent RANS and VLES: A review," *AIAA J.* **36**, 173 (1998).
- 21H. F. Fasel, J. Seidel, and S. Wernz, "A methodology for simulations of complex turbulent flows," *J. Fluids Eng.* **124**, 933 (2002).
- 22F. R. Menter, "Improved two-equation k-omega turbulence models for aerodynamic flows," Technical Memorandum No. NASA-TM-103975 (National Aeronautics and Space Administration, 1992).
- 23S. T. Bose and G. I. Park, "Wall-modeled large-eddy simulation for complex turbulent flows," *Annu. Rev. Fluid Mech.* **50**, 535 (2018).
- 24Ch. Friess, R. Manceau, and T. B. Gatski, "Toward an equivalence criterion for Hybrid RANS/LES methods," *Comput. Fluids* **122**, 233 (2015).
- 25P. Sagaut, *Large Eddy Simulation for Incompressible Flows: An Introduction* (Springer Science & Business Media, 2006).
- 26J. B. Perot and S. M. de Bruyn Kops, "Modeling turbulent dissipation at low and moderate Reynolds numbers," *J. Turbul.* **7**, N69 (2006).
- 27M. Germano, "Turbulence: The filtering approach," *J. Fluid Mech.* **238**, 325 (1992).
- 28J. A. Saenz, D. Aslangil, and D. Livescu, "Filtering, averaging, and scale dependency in homogeneous variable density turbulence," *Phys. Fluids* **33**, 025115 (2021).
- 29R. Schiestel and A. Dejoan, "Towards a new partially integrated transport model for coarse grid and unsteady turbulent flow simulations," *Theor. Comput. Fluid Dyn.* **18**, 443 (2005).
- 30M. Strelets, "Detached eddy simulation of massively separated flows," in 39th Aerospace Sciences Meeting and Exhibit, 2001.
- 31R. Bush and M. Mani, "A two-equation large eddy stress model for high sub-grid shear," AIAA Paper No. AIAA Paper 2001-2561, 2001.
- 32J. C. Kok, H. S. Dol, B. Oskam, and H. van der Ven, "Extra-large eddy simulation of massively separated flows," AIAA Paper No. AIAA Paper 2004-264, 2004.
- 33S. Heinz, "Unified turbulence models for LES and RANS, FDF and PDF simulations," *Theor. Comput. Fluid Dyn.* **21**, 99 (2007).
- 34C. De Langhe, B. Merci, and E. Dick, "Hybrid RANS/LES modelling with an approximate renormalization group. I: Model development," *J. Turbul.* **6**, N13 (2005).
- 35C. De Langhe, B. Merci, K. Lodefier, and E. Dick, "Hybrid RANS/LES modelling with an approximate renormalization group. II: Applications," *J. Turbul.* **6**, N14 (2005b).
- 36S. Heinz, "The large eddy simulation capability of Reynolds-averaged Navier-Stokes equations: Analytical results," *Phys. Fluids* **31**, 021702 (2019).
- 37P. Batten, U. Goldberg, and S. Chakravarthy, "Interfacing statistical turbulence closures with large-eddy simulation," *AIAA J.* **42**, 485 (2004).
- 38K.-J. Hsieh, F.-S. Lien, and E. Yee, "Towards a unified turbulence simulation approach for wall-bounded flows," *Flow, Turbul. Combust.* **84**, 193 (2010).
- 39X. Han and S. Krajnović, "An efficient very large eddy simulation model for simulation of turbulent flow," *Int. J. Numer. Methods Fluids* **71**, 1341 (2013).
- 40S. Ghosal *et al.*, "A dynamic localization model for large-eddy simulation of turbulent flows," *J. Fluid Mech.* **286**, 229 (1995).
- 41S. T. Johansen, J. Wu, and W. Shyy, "Filter-based unsteady RANS computations," *Int. J. Heat Fluid Flow* **25**, 10 (2004).
- 42F. F. Grinstein, J. A. Saenz, and M. Germano, "Coarse grained simulations of shock-driven turbulent material mixing," *Phys. Fluids* **33**, 035131 (2021).
- 43S. Bhushan and D. K. Walters, "A dynamic hybrid Reynolds-averaged Navier Stokes–Large eddy simulation modeling framework," *Phys. Fluids* **24**, 015103 (2012).
- 44S. Chen, Z. Xia, S. Pei, J. Wang, Y. Yang, Z. Xiao, and Y. Shi, "Reynolds-stress-constrained large-eddy simulation of wall-bounded turbulent flows," *J. Fluid Mech.* **703**, 1–28 (2012).
- 45M. Mortensen, "Shenfun: High performance spectral Galerkin computing platform," *J. Open Source Software* **3**, 1071 (2018).
- 46M. Mortensen and H. P. Langtangen, "High performance Python for direct numerical simulations of turbulent flows," *Comput. Phys. Commun.* **203**, 53 (2016).
- 47S. M. de Bruyn Kops and J. J. Riley, "Direct numerical simulation of laboratory experiments in isotropic turbulence," *Phys. Fluids* **10**, 2125 (1998).
- 48D. Livescu, F. A. Jaber, and C. K. Madnia, "Passive-scalar wake behind a line source in grid turbulence," *J. Fluid Mech.* **416**, 117–149 (2000).
- 49M. R. Petersen and D. Livescu, "Forcing for statistically stationary compressible isotropic turbulence," *Phys. Fluids* **22**, 116101 (2010).
- 50D. A. Donzis, P. K. Yeung, and K. R. Sreenivasan, "Dissipation and enstrophy in isotropic turbulence: Resolution effects and scaling in direct numerical simulations," *Phys. Fluids* **20**, 045108 (2008).
- 51F. Ilinca and D. Pelletier, "Positivity preservation and adaptive solution for the k-? model of turbulence," *AIAA J.* **36**, 44 (1998).
- 52See https://github.com/spectralDNS/spectralDNS/blob/master/demo/NS_shenfun.py for information about the Taylor-Green test case.